Dosimetric studies on the INTRABEAM electronic brachytherapy source

David Santiago Ayala Alvarez

Master of Science

Medical Physics Unit

McGill University

Montreal, QC

August 2019

A thesis submitted to McGill University in partial fulfillment of the requirement of the degree of Master of Science in Medical Radiation Physics

ACKNOWLEDGEMENTS

I am grateful to several people who have helped me in one way or another with the realization of this project. I want to thank my supervisor Dr. Jan Seuntjens for giving me the opportunity to join this world-renowned Medical Physics group, opening the doors for me and my wife to arrive in Canada and then trusting me as one of his students in his research group. I want to thank him for his support and guidance with his expertise in the field. He also ensured that I could have funding during my studies. I would like to thank Dr. Peter Watson for his help defining and shaping the project. His advice along the way has been crucial for this project, furthermore, he provided essential information for the INTRABEAM source modeling, valuable research content and bibliography. Thank you to Dr. Marija Popovic who taught me how to operate the INTRABEAM and introduced me to the clinical area where I performed the measurements. Thank you to the Radiation Safety Officer Michael Evans who helped me get access to the treatment rooms and provided tools required for radiation dosimetry and safety. Thank you to Dr. Tanner Connell, Dr. Piotr Pater, Dr. Monica Serban, Dr. Khushdeep Singh, Dr. Georges Al Makdessi, and other members of the clinic that helped me transport the INTRABEAM from the surgery rooms. Thank you to the engineers Joe Larkin and Bhavan Siva who built an accessory for measurements with the INTRABEAM arm without inclusion of applicators. Thank you to Gabriel Famulari for his important contributions in the dosimetric aspects of brachytherapy sources. I want to thank Felix Mathew, Veng Jean Heng, Chris Lund and José Alejandro Fragoso for their

friendship, support and advice to improve several aspects of the project and my performance in oral presentations. Thank you to Julien Mégrourèche for translating the abstract into French. Thank you to my colleagues and friends from the masters program that made this process a much better and enjoyable experience. Thank you to Margery Knewstubb and Tatjana Nisic for such a good work managing all the administrative matters. I would like to acknowledge partial support by the CREATE Medical Physics Research Training Network grant of the Natural Sciences and Engineering Research Council (Grant number: 432290).

I would like to express my gratitude to God for allowing me to reach this point and giving me the strength to move on. Finally, I would like to say thanks to my family. To my parents who shared with me this dream and are always there to encourage me. To my wife Lili, for always being there with me, being my best friend, and for her support along these years.

ABSTRACT

The INTRABEAM system is a miniature kilovoltage x-ray source manufactured by Zeiss (Carl Zeiss Meditech AG, Germany) and is designed especially for intraoperative radiotherapy applications. The nature of its use inside the patient body suggests its dosimetric study as an electronic brachytherapy source. As a brachytherapy source, the INTRABEAM represents a convenient alternative to conventional radionuclides since it delivers a low-energy (50 kVp) x-ray beam, reducing the regulatory and shielding requirements without compromising the dose delivery rates.

Despite its benefits and extended use for the treatment of brain and breast cancers, the source has not been characterized according to the AAPM TG-43 specifications, restricting its modeling in commercial treatment planning systems (TPS) for efficient dose calculations. In the present work, a brachytherapy dosimetry characterization of the INTRABEAM source based on the AAPM TG-43 protocol is presented.

The INTRABEAM source was modeled with Monte Carlo (MC) using egs_brachy, a user code of EGSnrc, which allows rapid dose calculations via a tracklength estimator. For the validation of the MC model, depth dose calculations in water along the source longitudinal axis were compared with measurements in a water phantom provided by the source manufacturer using a soft x-ray ionization chamber and two different INTRABEAM sources resulting in local differences lower than 10%, laying within the measurement uncertainties for points located at distances higher than

1 cm from the source tip, which represent the relevant situations for clinical cases. The suitability of an alternative radiation detector, a synthetic diamond (microDiamond from PTW) was assessed, resulting in a better performance than the air-filled ionization chamber at points close to the source tip where the high gradients in the dose distributions imply higher volume averaging effects for detectors with bigger radiation detection volumes.

Following the validation of the MC model, the TG-43 parameters were retrieved. The radial dose function diminished close to the source (< 1 cm) with a steep gradient higher than that of conventional brachytherapy radionuclides (^{192}Ir, ^{103}Pd and ^{125}I), but it is partially flattened at larger distances with a similar fall-off as the Xoft electronic brachytherapy source. The simulated polar anisotropy values were mainly uniform along $\theta = 0\,^{\circ}$ and gradually decreased close to the border of the source, affected by the beam attenuation in the elements of the source walls. The TG-43 parameters provided in this work serve as preliminary data required for tridimensional (3D) TPSs.

RÉSUMÉ

Le système INTRABEAM est une source miniature de rayons X en kilovoltage fabriquée par Zeiss (Carl Zeiss Meditech AG, Allemagne) et est spécialement conçu pour les applications de radiothérapie peropératoire. La nature de son utilisation dans le corps du patient suggère que son étude dosimétrique soit faite comme une source de curiethérapie électronique. En tant que source de curiethérapie, l'INTRABEAM représente une alternative pratique aux radionucléides conventionnels car il délivre un faisceau de rayons X à basse énergie (50 kVp), réduisant ainsi les exigences en matière de régulation et de protection sans compromettre les débits de dose.

Malgré ses avantages et son utilisation étendue pour le traitement du cancer du cerveau et du sein, la source n'a pas été caractérisée conformément aux spécifications de l'AAPM TG-43, limitant ainsi sa modélisation dans les systèmes commerciaux de planification de traitement pour un calcul efficace de la dose. Dans le présent travail, une caractérisation dosimétrique par curiethérapie de la source INTRABEAM, basée sur le protocole AAPM TG-43, est présentée.

La source INTRABEAM a été modélisée avec Monte Carlo (MC) en utilisant egs_brachy, un code utilisateur de EGSnrc, qui permet des calculs de dose rapides via un estimateur de longueur de "tracks". Pour la validation du modèle MC, les calculs de dose en profondeur dans l'eau, le long de l'axe longitudinal de la source, ont été comparés aux mesures faites sur un fantôme d'eau, fourni par le fabricant de la source, à l'aide d'une chambre d'ionisation à faible rayons X et de deux sources

INTRABEAM différentes. Des différences locales inférieures à 10%, comprises dans l'intervalle de confiance de mesures, ont été observées pour les points situés à des distances supérieures à 1 cm à partir de la source, correspondant à des situations pertinentes cliniquement. La pertinence d'un dosimètre alternatif, soit un diamant synthétique (microDiamond de PTW) , a aussi été évaluée. Les résultats obtenus ont montré de meilleures performances que ceux obtenus avec la chambre d'ionisation aux points proches de l'extrémité de la source, où les gradients élevés dans les distributions de dose impliquent des effets de moyennage volumique importants pour les détecteurs avec présentant un plus grand volume de détection.

Suite à la validation du modèle MC, les paramètres du TG-43 ont été obtenus. La fonction de la dose radiale a diminué près de la source (< 1 cm) avec un gradient plus grand que celle des radionucléides de curiethérapie classiques (^{192}Ir, ^{103}Pd and ^{125}I). Cependant, le gradient est partiellement aplati sur de plus grandes distances et présente une chute similaire à celle de la source de curiethérapie électronique Xoft. Les valeurs simulées d'anisotropie polaire étaient principalement uniformes le long de $\theta = 0\,^{\circ}$ et diminuaient progressivement près du bord de la source, en raison de l'atténuation du faisceau par les éléments des murs de la source. Les paramètres TG-43 fournis dans ce travail servent donc de données préliminaires pour les systèmes de planification de traitement tridimensionnels (3D).

TABLE OF CONTENTS

LIST OF TABLES

LIST OF FIGURES

LIST OF ABBREVIATIONS

1D, 2D, 3D: uni-, bi-, tridimensional
AAPM: American Association of Physicists in Medicine
CPE: Charged particle equilibrium
CT: Computed tomography
EBRT: External beam radiotherapy
EBT: Electronic brachytherapy
ECUT: Transport cut-off energy for electrons
EPOM: Effective point of measurement
FWHM: Full width at half maximum
Gy: Gray
HDR: High dose rate
HVL: Half value layer
IORT: Intraoperative radiotherapy
kV: Kilovoltage
kVp: Kilovoltage peak
LDR: Low dose rate
linac: linear accelerator
MC: Monte Carlo
MV: Megavoltage
NIST: National Institute of Standards and Technology
OAR: Organ at risk
PAICH: Probe Adjuster/Ionization Chamber Holder
PCUT: Transport cut-off energy for photons
PDA: Photodiode array
PDD: Percentage depth dose
QA: Quality assurance
RSV: Radiation-sensitive volume
SNR: Signal-to-noise ratio
SSD: Source to surface distance
TG: Task Group
TPS: Treatment planning system

CONTRIBUTION OF AUTHORS

Some results and data presented in this thesis are included in a manuscript that is being prepared for submission. I am the first author of the paper, but the co-authors have reviewed and edited it. The manuscript is entitled *"Monte Carlo calculation of the TG-43 dosimetry parameters for the INTRABEAM electronic brachytherapy source"* and was presented at the *2nd International Conference on Monte Carlo Techniques for Medical Applications* in June, 2019. The contribution from authors is as follows:

- David Santiago Ayala Alvarez: First author of the manuscript, performed the simulations, measurements and data analysis.
- Dr. Jan Seuntjens: Provided guidance and helped defining the project objectives and provided his expertise and follow up with measurements and simulations.
- Dr. Peter G. F. Watson: Provided initial codes and modeling of the INTRABEAM source, as well as his expertise and follow up with measurements and simulations.
- Dr. Marija Popovic: Assisted developing the conception of the project and provided guidance and support for the experiments.

Chapter 1
Introduction

1.1 Cancer and Radiotherapy

The term cancer is a global concept that encompasses several types of diseases which have in common their origin based on an abnormal growth and replication of cells caused by an alteration in the genetic code present in the DNA [1]. The Global Burden of Cancer (GLOBOCAN) from the International Agency for Research on Cancer estimated 18.1 million new cancer cases and 9.6 million cancer deaths in 2018. Female breast cancer, the most relevant in this thesis, has also the highest incidence worldwide [2].

According to the Canadian Cancer Society, 50% of Canadians are expected to be diagnosed with cancer at some point of their lifetime and 20% are expected to die from the disease [1]. Although these numbers have increased in recent years, it has been due to aging and increase of the population. However, it has been reported that risk rates have decreased thanks in part to new advances in early diagnosis and treatment methods and tools. Different cancer treatment modalities exist, among which the most commonly used are surgery, chemotherapy and radiotherapy (*a.k.a.* radiation therapy). The selection of the appropriate technique depends on many factors such as for example the type and extent of the cancer, and the different modalities can be used alone or in combination of them to improve the treatment outcome.

More than half of cancer patients undergo radiotherapy at some point during their treatments [3]. With radiotherapy, high-energy particles deposit energy to the cancer cells by means of ionizations and excitation of their atoms. These ionizations will subsequently damage the DNA molecules, through direct or indirect pathways, causing cell death either by inactivation of the cellular functions or by impeding their ability to reproduce. Because radiation interacts with tumoral and surrounding healthy cells, a trade-off between the tumour control and the detriment of the local healthy organs is required. Radiation doses that can be tolerated by the organs at risk close to the tumour and the required doses to achieve a therapeutic control of the tumor itself are determined from preclinical data collected from medical experience and clinical trials for different anatomical regions, tumour stage, age of the patient and other factors. This trade-off between the maximization of the tumor control probability and the minimization of the normal tissue complication probability is called the therapeutic window and is determined for each specific radiotherapy application [4].

1.2 Radiotherapy Modalities

Delivering the highest radiation doses to tumors while sparing the surrounding healthy tissues represents one of the main challenges for radiotherapy applications. In this context, different radiotherapy modalities have been developed and the correct selection of one of them is case-specific. These modalities can be currently split in two major classifications: external beam radiotherapy (EBRT) and brachytherapy.

1.2.1 External Beam Radiotherapy

With external beam radiotherapy, high-energy beams are directed into the tumour from outside the patient body using a machine. Nowadays, the most common machine employed in this type of treatments is the linear accelerator (linac). In a medical linac, electrons are accelerated to kinetic energies ranging from 4 to 25 MeV using a microwave field inside an evacuated cavity called accelerating waveguide. The accelerated electron beam can be used directly for therapies with electrons or can be made to collide with a material of high atomic number Z, called the x-ray target, in order to produce x-ray photons in the megavoltage (MV) range of energies between 4 to 25 MV as a result of bremsstrahlung emissions in which the electrons are decelerated by Coulomb interactions with the nuclei of the target liberating part of their kinetic energy in the form of photons [5].

Although treatments with high-energy particles predominate in external beam radiotherapy, low-energy (superficial) and medium-energy (orthovoltage) kilovoltage (tube potential: 40–100 kV) x-ray units are suitable for treatment of superficial lesions like skin cancer, keloids, surgical margins boost, among others [6, 7]. In medical kilovoltage units, electrons are accelerated from an electron source, the anode, towards a target electrode, the cathode, inside an evacuated tube, driven by a high intensity electric field generated by a high voltage set between the electrodes. Electrons in the cathode are produced by thermionic emission when an electric current heats the cathode filament. The anode contains a high-Z material where electrons lose part of their kinetic energy by bremsstrahlung emission as mentioned for megavoltage beams. However, a second form of x-ray emissions becomes relevant in the

energy spectrum of kilovoltage units represented by a set of peaks at specific energy values added to the continuous bremsstrahlung spectrum. This component of the spectrum is known as the characteristic x-rays, as they are dependent on the target material. Characteristic x-rays occur when electrons from a shell of the anode atoms occupy the vacancy left for electrons at a higher binding energy shell. These vacancies are created by collisional interactions of the incoming electrons from the cathode with the electrons in the inner shells of the target atoms [8]. The kilovoltage x-ray beams are less penetrating than megavoltage beams thus they deposit most of their energy closer to the surface of the body, reducing the radiation doses received by healthy tissues at higher depths. Figure 1–1 illustrates the differences in the deposition of energy from several x-ray beams in the kilovoltage and megavoltage energy ranges. The graph shows the percentage depth dose (PDD) in water for a kilovoltage 120 kV x-ray beam and compares it with the PDDs for megavoltage x-ray beams of 6, 10 and 15 MV. The kilovoltage x-ray beam was obtained using a GULMAY MEDICAL D3225 orthovoltage unit at the Jewish General Hospital and the megavoltage beam profiles were obtained from a Varian Truebeam linear accelerator located at the McGill University Health Centre.

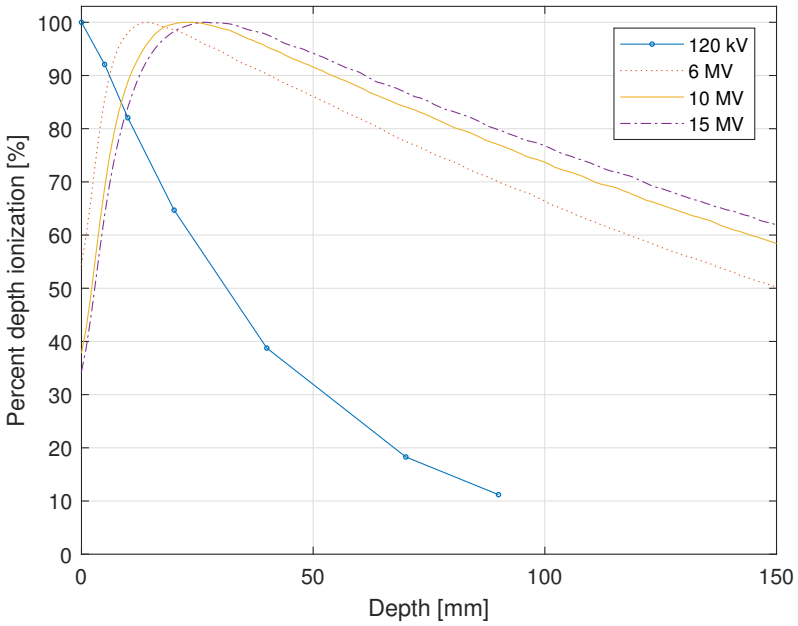

Figure 1–1 – Percentage depth dose curves for beams at the kilovoltage energy of 120 kV (continuous-dotted blue) and megavoltage energies of 6 MV (dotted red), 10 MV (continuous yellow) and 15 MV (dash-dotted purple).

It is clearly shown in Figure 1–1 that the maximum dose delivered by the kilovoltage unit is located at the surface of the body with a rapid dose falloff in depth, whereas for the more penetrating megavoltage beams a build-up in dose is observed at the entrance of the beam with a maximum dose delivery at few centimeters from the surface and a slower decrease in energy deposition at depth.

1.2.2 Brachytherapy

A second major type of radiotherapy applications consists of the placement of sources of radiation inside the tumor or in close proximity to it. This treatment modality is called brachytherapy and can be used in interstitial (through needles

inside the tumour), intracavitary (in natural body cavities) or superficial delivery modes [7]. Approximately 20% of radiotherapy patients are treated with brachytherapy [5]. Compared to external beam radiotherapy, brachytherapy procedures allow a better conformation of the dose distribution to the tumour while sparing the nearby organs at risk. According to the dose delivery rate at a reference point of treatment with radionuclides, brachytherapy applications can be classified as low dose rate (LDR) (0.4–2 Gy/h), medium dose rate (2–12 Gy/h) and high dose rate (HDR) (>12 Gy/h). Different radionuclides can be used for brachytherapy applications and most of them emit photons. Some examples of commonly used radionuclides in brachytherapy include iridium-192 (^{192}Ir) for HDR applications, and iodine-125 (^{125}I) and palladium-103 (^{103}Pd) for LDR applications. Table 1–1 presents some relevant information of the aforementioned radionuclides. In this table, the half-life indicates the period of time in which the number of radioactive nuclei from the source decays to half its initial value. The half value layer (HVL) is related to the penetrability of the beam produced by the source photon emissions and will be explained in detail in Chapter 2.

Table 1–1 – Examples of radionuclides commonly used in brachytherapy (Data from [5]).

Radionuclide	Half-life [days]	Average photon energy [MeV]	HVL in Pb [mm]
^{192}Ir	73.8	0.38 (0.14–1.06)	3
^{125}I	59.4	0.028	0.02
^{103}Pd	17.0	0.021	0.01

1.2.3 Intraoperative Radiotherapy

In intraoperative radiotherapy (IORT), a high single dose of radiation is delivered to the cavity left by primary tumours after being removed during surgery. IORT applications can be performed with electron beams or kilovoltage photon beams [9]. This novel technique flourished in the 1970s and 1980s with the advent of mobile radiotherapy devices and was proved to be a good alternative over conventional megavoltage EBRT for tumours close to critical organs at risk, allowing an otherwise prohibited escalation of radiation doses delivered to the tumour bed, minimizing the morbidity to surrounding healthy tissues which can even be moved away from the radiation beam [10]. Treatments with IORT started with cases of rectal and pancreatic cancer, thoracic tumours, retroperitoneal sarcoma, and some gynecologic and genitourinary malignancies. However, the limited number of these cases restricted the evaluation of IORT in phase III clinical trials, with the exception of breast cancers [11], for which the higher incidence allowed more rigorous studies.

Some representative clinical trials evaluating the performance of IORT include the TARGIT-A trial, launched in 2000, in which the local cancer recurrence and overall survival for treatments of breast cancer boosts using IORT was compared with external beam radiotherapy as the gold standard. The results of the study at five years showed a non-inferiority of IORT. The new technique was favorable in terms of logistics (one single dose *vs* 25 fractions with the conventional EBRT) [12]. In 2014, a different phase I/II clinical trial, the INTRAGO [13], was conducted to evaluate the safety and tolerability of IORT in glioblastoma multiforme, the most common primary malignant brain tumours in adults. The results showed that IORT

treatments provide long-lasting local control and the technique proved to be safe and efficient in brain tumours [14].

Different techniques and tools can be employed in the application of IORT. High-energy electron beams use a mobile linear accelerator with specialized cones to collimate the beam into the tumour bed. Photons can be delivered using conventional HDR brachytherapy applicators and radionuclides such as ^{192}Ir and ^{60}Co. Low-energy x-rays ($\sim$50 kVp) can be also obtained with miniature x-ray generators [15]. The TARGIT-A and the INTRAGO protocols for IORT used the INTRABEAM (Carl Zeiss Meditec AG) which is a miniature kilovoltage x-ray generator that can be introduced into the tumour bed in a similar way as a brachytherapy source. The use of these types of sources is understood under the technique sometimes labeled as electronic brachytherapy (EBT).

1.2.4 Electronic Brachytherapy

Due to the high complexity of IORT procedures and thanks to recent advances in radiotherapy devices, EBT was introduced and has been gaining space in the radiotherapy market as a convenient alternative to conventional brachytherapy with radionuclides [16]. EBT sources are miniature x-ray generators that operate at low kilovoltage energy ranges ($\sim$50 kVp). The low energies of the technique and the absence of radioactive sources reduce the regulatory and shielding requirements and increases the radiobiological effectiveness [17]. In addition, the portability of the system allows its easy transportation between surgery rooms where IORT procedures are performed without the need of bringing the patient with an open wound to a static linac.

The first systems encompassed by the definition of EBT and that represent its main commercial examples nowadays are the INTRABEAM system (Carl Zeiss Meditec AG, Jena, Germany) and the Xoft Axxent^{TM} system (iCAD Inc., Nashua, NH). The INTRABEAM system contains a miniature linear accelerator that moves electrons towards a gold target where 50 kVp x-rays are produced. This system will be described in more detail in the next sections. On the other hand, the Xoft source was released in 2006 and contains a flexible sheath surrounding the miniature x-ray tube, which is internally cooled with water during operation. The device is also capable of generating x-rays of energies up to 50 keV [18, 19]. Unlike the INTRABEAM, the Xoft source has a limited lifetime of approximately 3 h [17]. The Xoft source contains a tungsten target instead of a gold target and this feature, together with the different filtration used, produces an energy spectrum with higher energy peaks due to characteristic x-rays, mostly observed close to the source. As a result, the average energy at the Xoft source surface is higher than that of the INTRABEAM, making the Xoft beam more penetrating.

1.3 INTRABEAM System

The INTRABEAM system was initially developed in the 1990s for interstitial radiosurgical treatments of intracranial cancer metastases [20]. With the inclusion of new applicators for the source, the system use was expanded to treat other sites such as rectal cancer and peripheral soft tissue sarcomas, and since 1998 to nowadays it is mainly employed for the treatment of breast cancer patients with IORT [21]. Figure 1–2 shows on the left the INTRABEAM source with a spherical applicator mounted in an arm especially designed to allow precise motion and positioning of the system

into the tumour bed and, on the right, a schematic of the INTRABEAM x-ray tube indicating the internal components used in the beam formation and transport.

1.3.1 INTRABEAM Basics and Components

With the INTRABEAM system, electrons produced in an electron gun are accelerated to an energy of 50 keV. The electrons are then transported in vacuum towards the tip of an evacuated metallic probe where approximately 50 kVp x-rays are produced by bremsstrahlung and fluorescence in a gold target located at the inner cavity of the source tip [22, 23]. The electron beam is internally deflected in the evacuated needle using a magnetic beam deflector, producing a nearly isotropic dose distribution around the probe tip [24, 25, 26].

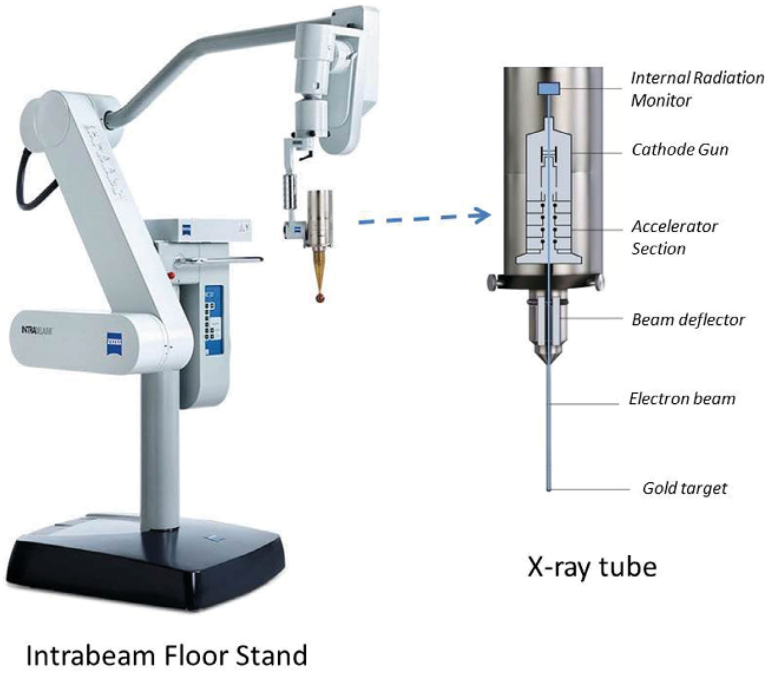

Figure 1–2 – INTRABEAM system with a spherical applicator mounted on a floor stand. On the right, a schematic of the x-ray tube indicates the internal components for the beam formation and transport (image taken from [27]).

The INTRABEAM system allows the use of different applicators for a variety of lesions and anatomical sites. For instance, spherical applicators are used for brain and breast tumours, flat and surface applicators for superficial skin cancers, spinal applicators for vertebral bodies, and cylindrical applicators for vagina in patients with endometrial cancer [21]. The most commonly used are the spherical applicators which range in diameter from 1.5 to 5.0 cm in steps of 0.5 cm. Figure 1–3 shows a picture of a 4 cm diameter spherical applicator. These applicators are placed on the INTRABEAM source in a way that the source tip is fixed at the sphere center. The material they are made of is a biocompatible polyetherimide with an internal air gap where the source is inserted [28]. The smallest applicators (<3.5 cm) include an aluminum filter required for the source to produce an homogeneous dose distribution at the applicator surface.

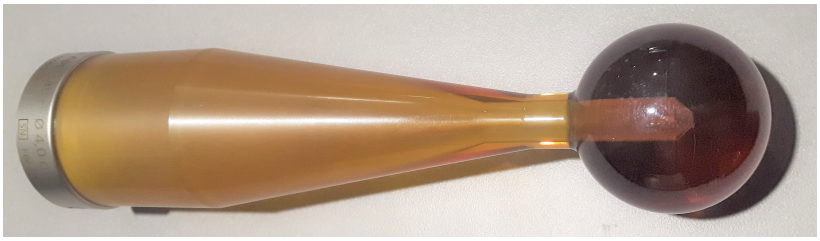

Figure 1–3 – Spherical applicator of 4 cm diameter used with the INTRABEAM system for IORT in breast and brain tumours.

The system includes a control console where the treatment parameters are set and monitored, and this is connected to a user terminal where the treatment parameters and different quality control tests are verified [29].

1.3.2 INTRABEAM System Workflow and Quality Assurance

As established in 1993 by the American Association of Physicists in Medicine (AAPM) [30], it is the responsibility of the clinical medical physicist in radiotherapy to ensure that radiation sources perform as expected by means of acceptance tests and commissioning at the time of acquisition and during periodic controls after that. The physicists must assure that the sources are calibrated and the measurement equipment and treatment planning software are verified and optimized in order for the equipment to deliver prescribed doses and dose distributions within acceptable degrees of accuracy.

The INTRABEAM system includes several tools and procedures that help the physicist verify the value and constancy of the radiation doses delivered by a specific source before its use in patient treatments. As shown in Figure 1–2, the x-ray source contains an internal radiation monitor that allows the system to verify the dose rate constancy by measuring the dose from x-ray photons back-scattered from the gold target up through the evacuated needle [29]. In order to measure and check the isotropy of the dose distribution around the source, the system includes a device called the Photodiode Array (PDA) that contains five diodes at orthogonal directions from the source tip. The PDA allows the system to tweak the internal electron beam deflection for improved isotropy. In addition to the PDA, the Probe Adjuster/Ionization Chamber Holder (PAICH) verifies the straightness of the source needle and contains an opening to insert a PTW 23342 soft x-ray ionization chamber that serves to measure the radiation output of the beam at a reference position. Deviations on the output measured with the PAICH are corrected by the INTRABEAM

system by modifying the irradiation time. Once the quality assurance (QA) tests are performed using the previously described QA tools, the INTRABEAM source is mounted on the arm and is connected to a sterilized applicator. The source is covered with a sterile drape before insertion in the tumour bed [29].

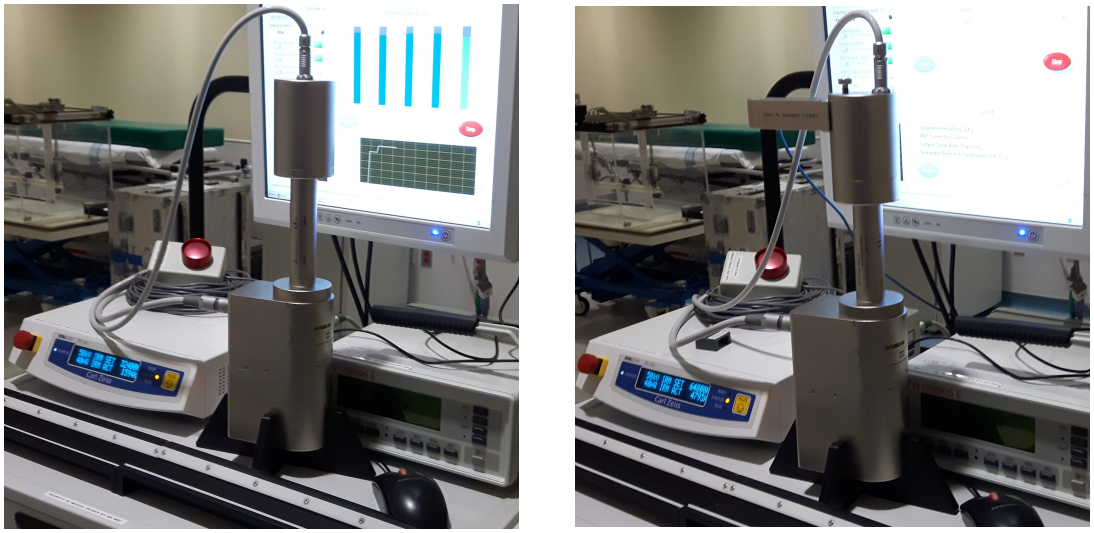

(a) PDA (b) PAICH

Figure 1–4 – Photodiode Array (PDA) (a) and Probe Adjuster/Ionization Chamber Holder (PAICH) (b) set on the INTRABEAM source for QA tests. Pictures show in the background the control console, the user terminal and a PTW UNIDOS E electrometer where the ionization chamber is connected for output verification with the PAICH.

The manufacturer of the source (Carl Zeiss, Germany) provides calibration depth dose curves that make it possible to determine the dose distribution at different depths in water along the source axis. The depth dose curves must be corrected for each applicator using transfer functions also provided by the manufacturer and can be verified by measuring with a PTW 34013A ionization chamber and a water phantom available from Zeiss [27, 31]. Treatment plans with the INTRABEAM system for

IORT generally consist of the determination of treatment times required to achieve a dose prescribed by the physician at the depth of the tumour using look-up tables available from the Zeiss calibration for the specific source.

It is part of the role of clinical medical physicists to perform dosimetric measurements for radiation sources independent from the calibration by the manufacturer [32]. In the past two years, Watson *et al.* [33, 34] developed a protocol to independently determine the absorbed dose to water from the INTRABEAM source using a Monte Carlo (MC) calculated factor (C_Q) and validated their results with depth dose measurements using a soft x-ray ionization chamber and radiochromic film dosimetry.

1.4 Thesis Motivation and Objectives

Independent dosimetry protocols traceable to primary standards for electronic brachytherapy sources are recently investigated and constitute an open field of research. As discussed in Section 1.3.2, Watson *et al.* [33] developed a method for determining the absorbed dose to water from the INTRABEAM electronic brachytherapy source using a soft x-ray ionization chamber. However, they found that their MC calculated C_Q correction factor is highly dependent on the geometry of the ionization chamber and the PTW 34013A soft x-ray ionization chamber that was used in the experiments has high uncertainties in geometry aspects as the plate separation, thus suggesting further research with alternative radiation detectors.

The current INTRABEAM system only provides the dose to a specific point or along a depth dose curve. A method that allows the acquisition of 3D dose distribution data transferable to conventional TPSs is desired. In this context, in 2006, Rivard et al [18] studied the brachytherapy parameters obtained from the Xoft

(iCAD Inc., Nashua, NH) electronic x-ray source using a modified version of the AAPM TG-43 protocol that allows the acquisition of 3D dose distributions in water from the source [35, 36]. For the INTRABEAM source, the TG-43 parameters are to our knowledge non-existent.

The present work addresses the aforementioned issues with the INTRABEAM dosimetry as summarized in the following thesis objectives:

1. To obtain the TG-43 dosimetry parameters for the INTRABEAM source, using Monte Carlo (MC) simulations, that can be used in commercial TPSs for efficient dose calculations in IORT. The air kerma rate calibration of the source is not addressed in this thesis.
2. To validate the MC simulations of the source and, therefore, of the obtained TG-43 parameters, by measuring in water with the PTW 34013A soft x-ray ionization chamber and with an alternative radiation detector with better geometry definition.

Chapter 2 of this thesis presents the theory behind the dosimetry of radiation sources and establishes the basis of knowledge required to understand the methods employed on the INTRABEAM dosimetry and for the analysis of the results obtained. Chapter 3 describes in detail the materials and methods used to address the thesis objectives outlined above. Subsequently, Chapter 4 outlines the results and the discussion drawn from them. Finally, Chapter 5 will conclude this work with a summary and provides an overview of new challenges and future work to be performed.

Chapter 2
Theory

As discussed in Chapter 1, one of the main goals of radiation therapy is to deliver the maximum amounts of radiation doses to tumoral cells but minimizing the detriment of the nearby healthy tissues. It is crucial to establish universal consensus on dosimetry quantities and units that allow an understanding of the required 'amounts' to effectively control the tumour and define those constraints tolerated by organs at risk.

In the following sections, an overview of the basic concepts and quantities used in radiation dosimetry is presented, followed by a description of the design and operation of some radiation detectors. Then, a review of relevant dosimetry protocols for kilovoltage photon beams will be discussed, and the protocols and concepts employed in the dosimetry of the INTRABEAM system will be detailed. The chapter concludes with the introduction of Monte Carlo calculations and the description of variance reduction techniques employed in this work.

2.1 Dosimetric Quantities and Concepts

The interactions of ionizing radiation with matter depend on the radiation particles, beam energies and composition of the tissues found in the trajectories of beam particles. These interactions will deposit energy in the media by means of excitations and ionizations of the tissue atoms. The ultimate purpose of radiation dosimetry is

to determine the energy absorbed by the tissue as a result of these multiple interactions, since is the absorbed energy that is responsible for the biological effects of radiation. The definitions and units of most fundamental quantities used in radiation dosimetry are summarized in the Report 85 (2011) of the International Commission on Radiation Units and Measurements [37]. Some of these quantities and concepts that are relevant for the understanding of the INTRABEAM dosimetry are explained below.

2.1.1 Radiation Quality

One important component in the characterization of a radiation beam is called the radiation *quality* which defines the radiation's ability to penetrate in materials of known composition [7]. A complete characterization of an x-ray beam would include an energy spectrum at different positions in tissue, but spectral measurements are cumbersome and usually not necessary to specify quantities of dosimetric interest. As will be discussed later, the tube potential (peak tube voltage, kVp) and the *half value layer* (HVL) used together to specify the beam, are the most important beam quality specifiers in x-ray devices of energies in the range of superficial and orthovoltage beams [6].

According to the Beer-Lambert law, attenuation of the intensity of a monoenergetic photon beam as it traverses an attenuating material is described as a function of thickness of the attenuating material x, by the exponential function,

$$I = I_0 \cdot e^{-\mu x}, \tag{2.1}$$

where I_0 is the intensity of the unattenuated beam and μ corresponds to the *linear attenuation coefficient* [8]. The first HVL (HVL_1) corresponds to the thickness of a specific material that reduces the intensity (or *air kerma rate*) of the studied beam to half its initial value, when measured in a narrow beam geometry. HVL can be specified in terms of "mm Al" for low-energy beams (tube potential: 40 kV–100 kV), but its use is sometimes extended to beam energies up to 150 kV [6]. From Eq. 2.1, the HVL_1 is then the value of x when $I/I_0 = 1/2$,

$$HVL_1 = \frac{\ln(2)}{\mu}. \tag{2.2}$$

Attenuation is dependent on the attenuator density ρ, thus Eq. 2.1 can be expressed as

$$\frac{I}{I_0} = e^{-(\mu/\rho)\rho x}, \tag{2.3}$$

where I/I_0 is the transmission ratio, and μ/ρ is called the *mass attenuation coefficient*. After being attenuated, the thickness of attenuating material for monoenergetic beams to further reduce the beam intensity to half its value remains constant. For most clinical cases, beams are polyenergetic, thus subsequent HVLs may increase due to *beam hardening*, or decrease due to *beam softening*.

From Eq. 2.3 and the definition of HVL_1,

$$\left(\frac{\mu}{\rho}\right)_{\text{eff}} = \frac{ln(2)}{\rho(HVL_1)}, \tag{2.4}$$

where $(\mu/\rho)_{\text{eff}}$ is the effective mass attenuation coefficient obtained from the first HVL of a polyenergetic beam. The first HVL can be also used to determine a beam quality specifier for polyenergetic beams called the *effective energy* [8], which corresponds

to the energy of a monoenergetic beam that produces the same first HVL as the specified beam. The effective energy is usually 30 to 40% of the maximum energy value.

2.1.2 Photon Interaction Coefficients

In a photon beam traversing a medium, the proportion of the energy that is transferred from the photons to the attenuating material of density ρ, in the form of kinetic energy to charged particles, is called the *mass energy transfer coefficient* (μ_{tr}/ρ) with SI units of $\text{cm}^2\ \text{g}^{-1}$ [7]. This coefficient is expressed in terms of μ/ρ as

$$\frac{\mu_{\text{tr}}}{\rho} = \frac{E_{\text{tr}}}{h\nu}\frac{\mu}{\rho}, \tag{2.5}$$

where E_{tr} is the mean energy per interaction transferred to charged particles of the medium, and $h\nu$ is the energy of the incoming photons.

Some of the electrons put in motion will expend their kinetic energy in inelastic collisions with other electrons of the medium, but some others will lose part of their energy by coulomb interactions with nuclei of the material, emitting bremsstrahlung x-rays that will not deposit their energy in the local volume and will not contribute to the local absorbed energy. The proportion of the energy locally absorbed in the medium of density ρ is defined as the *mass energy absorption coefficient* (μ_{en}/ρ) with SI units of $\text{cm}^2\ \text{g}^{-1}$ and is expressed in terms of μ_{tr}/ρ as

$$\frac{\mu_{\text{en}}}{\rho} = \frac{\mu_{\text{tr}}}{\rho}(1-g), \tag{2.6}$$

where g is the fraction of the transferred energy that is lost by the electrons in form of radiation.

2.1.3 Kerma

The *kerma* (kinetic energy released per unit mass), K, is defined as the quotient of dE_{tr} by dm, where dE_{tr} is the mean sum of the initial kinetic energies of all charged particles liberated in the mass dm by incident uncharged particles [38],

$$K = \frac{dE_{\text{tr}}}{dm}. \tag{2.7}$$

The SI unit for kerma is J kg^{-1}, which for kerma has been given the special name of gray (Gy).

For a polyenergetic photon fluence spectrum, kerma can be obtained with an integral over the energy fluence spectrum as

$$K = \int \Phi_E E \frac{\mu_{\text{tr}}}{\rho} dE = \int \Psi_E \frac{\mu_{\text{tr}}}{\rho} dE, \tag{2.8}$$

where $\Phi_E E$ is the distribution with respect to the energy of the *fluence* of uncharged particles, and Ψ_E is the distribution of *energy fluence*.

As observed in Eq. 2.8, kerma is expressed in terms of fluence, meaning that it can be defined for a specific material at a point inside a different material. An example is *air kerma* in water, which has important implications in dosimetry protocols for low energy photon beams.

The *electronic kerma* (K_{el}), also known as collision kerma, encompasses only the portion of kerma resulting in charged particles absorption in the local volume, excluding radiative losses as bremsstrahlung or annihilation in flight [37]. For a distribution with respect to energy, Ψ_E, of uncharged-particle energy fluence, electronic

kerma can be obtained from

$$K_{\mathrm{el}} = \int \Psi_E \frac{\mu_{\mathrm{en}}}{\rho} dE = \int \Psi_E \frac{\mu_{\mathrm{tr}}}{\rho}(1-\bar{g})dE = K(1-\bar{g}), \tag{2.9}$$

where $\bar{g}$ represents the average value of the radiative losses, g, over the distribution of kerma with respect to the electron energy.

2.1.4 Absorbed Dose

The *absorbed dose*, D, is defined as the quotient of $d\bar{\epsilon}$ by dm, where $d\bar{\epsilon}$ is the mean energy imparted by ionizing radiation to the mass dm [37],

$$D = \frac{d\bar{\epsilon}}{dm}. \tag{2.10}$$

The mean energy imparted, $d\bar{\epsilon}$, includes the mean radiant energy of all charged and uncharged particles entering a volume of interest, subtracting the mean radiant energy of all particles leaving the volume, plus the mean sum of all the changes in the rest energy of nuclei and particles inside the volume.

The absorbed dose is determined at any point by considering the limit when dm approaches zero, and constitutes the most relevant quantity in radiation dosimetry. The SI unit for absorbed dose is J kg^{-1}, which for dose receives the special name of gray (Gy).

2.1.5 Charged Particle Equilibrium

The kerma and the absorbed dose concepts make reference to a specific volume of interest, v. It should be noted that the secondary charged particles generated by photons might deposit part of their energy in v and part of it outside v, thus affecting the relation between electronic kerma and absorbed dose. If the radiant energy from

charged particles entering the volume v equals the radiant energy leaving v, then a condition of *charged particle equilibrium* (CPE) exists [38]. For the situation of CPE, absorbed dose will be equal to the electronic kerma and can be determined as

$$D = K_{\text{el}} = \int \Psi_E \frac{\mu_{\text{en}}}{\rho} dE. \tag{2.11}$$

For the case of low energy photons, most of the secondary charged particles generated will not travel far and will deposit their energy locally. The energy range to enclose "low energy" photons depends on the application. In the context of radiotherapy and radiobiology, the AAPM's TG-61 protocol classifies as low energy photons those produced by tube potentials lower or equal to 100 kV [6]. In This energy range, radiative losses are usually negligible and kerma can be approximated by electronic kerma. When adding the CPE condition, the absorbed dose will be essentially kerma

$$D = K_{\text{el}} = K. \tag{2.12}$$

It is worth mentioning that at high photon energies, absorbed dose and kerma become higher than electronic kerma and Eq. 2.12 cannot be applied.

2.2 Radiation Dosimeters

A radiation dosimeter is an instrument that can measure, in a direct or indirect way, ionizing radiation quantities delivered to a medium. The dosimetric quantities of major interest for this thesis are the absorbed dose and kerma, or their respective time derivatives. These quantities are usually obtained in an indirect way by means of measuring, within the radiation-sensitive volume (RSV) of an appropriate detector, a physical property that correlates with the energy imparted to the RSV, as for

example electrical charge, heat transfer, chemical reactions, light emission, among others, and then applying a range of correction and conversion factors [5, 38].

In order to obtain a reliable measurement, radiation detectors must satisfy certain properties. Depending on the application for which the dosimeter will be employed, some of the properties to be evaluated are linearity, reproducibility, dose range, dose-rate range, stability, energy dependence, directional dependence, and spatial resolution. The *linearity* of the detector indicates that the measured signal is proportional to the quantity of interest within the dose range of interest. The *reproducibility* or *precision* makes reference to the magnitude of the random errors of the measurements due to, e.g., ambient conditions, fluctuations in the instrument itself, etc, and can be usually determined as the standard error on the mean of a set of repetitive measurements. The *dose range* indicates that the dosimeter should respond with a detectable and reproducible signal within the intended dose range of the application. Similarly, the *dose-rate range* encompasses the performance of the detector in terms of its response in a required dose-rate range, which should be unaffected by expected dose-rate variations. The *stability* indicates how the dosimetric characteristics of the detector are kept invariant with time before, during and after its use in radiation measurements; some types of integrating dosimeters such as films and solid-state detectors can be unstable in between the irradiation and readout, with some fading effects that can be accounted for in dosimetry protocols. The variations of the response of a dosimeter in terms of radiation beam quality is evaluated in its *energy dependence*. The ideal situation is a flat response with energy variations, but this is usually not the real situation and then, correction factors from

the response at the calibration beam to the intended beam quality must be used. The *directional dependence* of the dosimeter makes reference to the different response obtained depending on the direction in which the incident beam reaches its RSV and is associated with the detector construction characteristics that might favor a specific orientation of use but might not be suitable for other applications. An ideal dosimeter should be able to measure the dose to a point. This is not achieved in practice because of the limitations on the minimum achievable physical dimensions of the RSV that permits an acceptable signal to noise ratio (SNR) on the reading. The *spatial resolution* quantifies the minimum volume for which the dose can be measured with the detector [5, 38]. The finite size of the RSV must be considered when choosing the detector for measurements in regions of high dose gradients because *volume averaging* effects might significantly affect the accuracy of the dose readings [39].

Different types of radiation dosimeters exists that can be classified according to their physical properties and composition of their RSVs. Namely, there are four major groups for their use in radiation dosimetry: (1) calorimeters (e.g., water and graphite); (2) ionization chambers (e.g., air, gas or liquid filled ion chambers); (3) chemical detectors (e.g., radiographic and radiochromic films, fricke dosimeters and gel dosimeters); and (4) solid state detectors (e.g., thermoluminescent dosimeters, optically-stimulated luminescence dosimeters, scintillation detectors, silicon diodes and diamond detectors). Due to the specific physics and design properties of interest in the dosimetry of the INTRABEAM system, the properties of air-filled ionization

chambers and solid state diamond detectors are the only systems that will be discussed in more detail. The reader is referred to additional bibliography for details about other detectors [5, 38].

2.2.1 Ionization Chambers

Ionization (or ion) chambers are the most commonly used examples of radiation dosimeters. Their general design includes a gas (usually air) filled cavity with a pair of electrodes connected to a polarizing high voltage that generates an electric field between them. The electric field moves the ion pairs generated by ionization of the atoms of the gas in the RSV as a result of the interactions of incoming ionizing radiation. The transport of charges through an electrode (collecting electrode) produces an electric current that is proportional to the radiation doses deposited inside the gas cavity, thus allowing an indirect absorbed dose measurement. Some ion chambers have an open exchange of air with the exterior of the chamber and require corrections for changes in the mass of air in the cavity due to variations in the environment conditions relative to reference conditions from calibration, namely, the temperature and pressure. Other corrections include those for incomplete charge collection, polarization correction factors and the calibration coefficient determined at a standards laboratory. Also included in the design is an insulator material separating the electrodes outside the collecting region and a guard electrode is usually added to further reduce leakage currents between them and to ensure a homogeneous electric field in the RSV.

The concept of ionization chambers is simple, and their reproducibility and stability make of them versatile instruments of different sizes suitable for use in

a wide range of dose measurements. Primary standards laboratories typically use ionization chambers of large cavity volumes with the purpose of increase sensitivity. For low energy photons and high dose gradient regions, a small cavity size is desired for improved spatial resolution, losing in part the achievable SNR. Besides their size, the geometry of these detectors can also vary among cylindrical, spherical, parallel-plate, among other configurations [5, 38]. Because some favorable characteristics in their design and their extended use in low energy photons, the parallel-plate ionization chambers are evaluated in the dosimetry of the INTRABEAM system.

Parallel-Plate Ionization Chambers

In a parallel-plate (*a.k.a.* as plane-parallel) ionization chamber the electrodes are fixed to two parallel walls. The frontal electrode joins the entrance window of the chamber cavity and the back electrode is attached to the back wall and body of the chamber, generally made of a non-conductive material (usually a polystyrene) that provides a scatter setup designed to reduce the energy dependence of the dosimeter in kV beams [5, 38]. The back electrode consists of the collecting electrode and a guard ring around the collecting electrode.

The design of parallel-plate ionization chambers makes them suitable for measurements in electron beams and in low energy photon beams, since they allow the use of thin entrance windows (mass thickness of a few mg cm^{-2}). The chambers used for low energy photon beams are called soft x-ray chambers. Figure 2–1 presents the scheme of a soft x-ray ionization chamber, the PTW (Freiburg, Germany) model 34013, evaluated in this work for its use for INTRABEAM dosimetry.

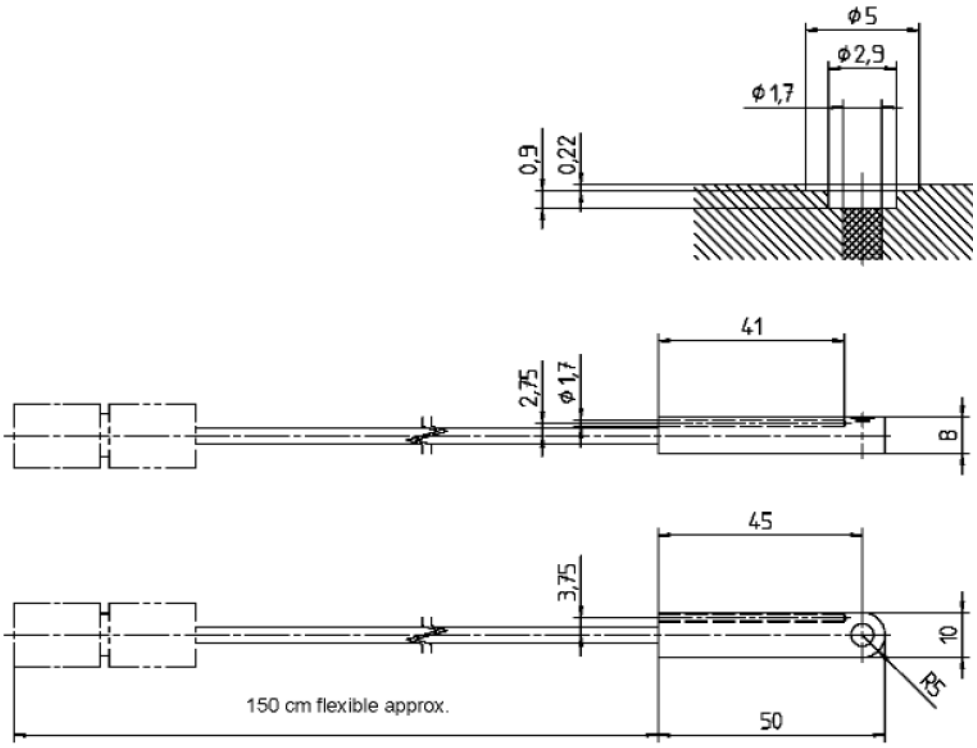

Figure 2–1 – PTW 34013 parallel-plate ionization chamber schemes. Details of the measuring volume are detailed in the inset on the up-right corner (image taken from [40]).

As shown in Figure 2–1, the 0.005 cm^3 nominal measuring volume is enclosed by the two electrodes forming a cylindrical volume of 1.45 mm radius and 0.9 mm thickness. The frontal electrode is attached to a 0.03 mm polyethylene (PE) entrance window of total area density of 2.76 mg cm^{-2}. The collecting electrode has a nominal diameter of 1.6 mm. These compact ionization chambers are used for low energy photons from 15 keV to 70 keV. The operating potential between electrodes is up to $\pm$ 400 V. In order to operate these chambers in a water phantom, a waterproofing sleeve is required [40].

Chamber Corrections for Influence Quantities

The measurements obtained with ionization chambers are affected by different factors that vary from the reference conditions at which the calibration coefficient was obtained. Ionization chambers with air communication are subject to changes in the amount of air molecules in the RSV depending on the environment temperature and pressure, and water molecules will change depending on the local humidity. Among with environment factors, the polarity and voltage between electrodes can affect the reading of the dosimeters. These factors affecting the measurement of ionization chambers are called the *influence quantities* and are included in the different ion chamber-based dosimetry protocols [6, 41, 42]. The most relevant influence quantities are described below.

Charge (or current) measurements with an ion chamber must be corrected according to

$$M = M_{\text{raw}} P_{\text{TP}} P_{\text{ion}} P_{\text{pol}} P_{\text{elec}}, \tag{2.13}$$

where M_{raw} is the uncorrected charge measurement; P_{TP} is a correction factor that accounts for variations in the mass of air in the sensitive volume due to the environmental temperature and pressure; P_{ion} refers to the effect of ions produced in the sensitive volume that recombine before being collected by the collection electrode; P_{pol} is the polarization correction factor that can be established from measurements in both source polarities; P_{elec} refers to the electrometer calibration correction factor.

The temperature and pressure correction factor is determined from the environmental and reference conditions as

$$P_{\mathrm{TP}} = \frac{P_{\mathrm{ref}}}{P} \cdot \frac{(T\,[^{\circ}C] + 273.2)}{(T_{\mathrm{ref}}\,[^{\circ}C] + 273.2)}, \tag{2.14}$$

where T and P are the values of temperature and pressure observed in the room at the time of the measurements. T_{ref} and P_{ref} are the corresponding reference values for that of the ion chamber calibration, with typical values of $T_{\mathrm{ref}} = 22\,^{\circ}C$, and $P_{\mathrm{ref}} = 101.33$ kPa.

The electrometer correction factor, P_{elec}, is applied to the charge measurement when the electrometer and the ion chamber are calibrated separately. This value corresponds to the electrometer calibration correction factor that converts the reading to charge in coulombs. When the ion chamber is sent to calibration in conjunction with the provided electrometer, P_{elec} can be considered unity ($P_{\mathrm{elec}} = 1.00$).

The recombination correction factor, P_{ion}, accounts for incomplete ion collection. These means that not all ion-pairs produced in the RSV will be collected in the collecting electrode but will recombine, before reaching the electrode, with other opposing sign ions produced. P_{ion} is obtained using a standard method called the two voltage technique that, for continuous beams, is given by

$$P_{\mathrm{ion}}(V_{\mathrm{H}}) = \frac{1 - (V_{\mathrm{H}} \,/\, V_{\mathrm{L}})^2}{M^{H}_{\mathrm{raw}} \,/\, M^{L}_{\mathrm{raw}} - (V_{\mathrm{H}} \,/\, V_{\mathrm{L}})^2}, \tag{2.15}$$

where V_{H} is the higher voltage corresponding to the normal operating voltage of the ion chamber, V_{L} is the reduced voltage value, and M^{H}_{raw} and M^{L}_{raw} are its corresponding charge measurements.

When using polarizing potentials between the chamber electrodes the effect of changing the polarity must be accounted for and might have a significant effect in electron and low energy photon beams. The correction factor P_{pol} is determined from the measurements at both polarities as

$$P_{\text{pol}} = \left| \frac{M^{+}_{\text{raw}} - M^{-}_{\text{raw}}}{2M_{\text{raw}}} \right|, \tag{2.16}$$

where M^{+}_{raw} and $-M^{-}_{\text{raw}}$ represent the measurements at positive and negative polarities and M_{raw} is set at the polarity used for the reference measurements.

2.2.2 Diamond Dosimeters

Natural Diamond Dosimeters

Diamond dosimeters are an example of solid-state radiation detectors. Natural diamonds can be employed as radiation dosimeters since they change their electric resistance when exposed to radiation. This property is a response of a set of impurities (N, B, Al, and others) contained in a carbon crystal that allows them to behave as a semiconductor material during irradiation [5, 38]. Diamonds have a low atomic number ($Z = 6$ for carbon) that is close to that of soft tissues ($Z = 7.4$) and, therefore, present a radiation response very close to that of water in a wide range of therapeutic options, including the kilovoltage x-ray beams [43]. This near-water equivalence combined with the property of being waterproof detectors, make diamonds interesting clinical radiation dosimeters suitable for use in water phantoms. In addition, diamonds exhibit high radiation dose sensitivity, low leakage current and a high resistance to radiation damage. Natural diamonds have a very thin sensitive volume (< 0.5 mm) associated to a low directional dependence and an excellent

spatial resolution, making them suitable candidates for measurements in high dose gradient regions.

Synthetic Diamond Dosimeters

Despite the previously mentioned advantages, natural diamonds require long pre-irradiation times to reduce polarization effects and exhibit high dose rate dependence, especially with low energy photon beams. Besides, appropriate natural crystals for dosimetry are difficult to find, expensive and not very reproducible. The development of a new synthetic diamond overcame some of the issues with the natural detector, by obtaining a highly reproducible crystal from chemical vapor deposition on a low-cost substrate [44]. However, the new model might require a density correction factor because of their mass density (3.52 g cm^{-3}) difference to that of water [38]. As in the case for silicon semiconductors, the synthetic diamond detectors do not require bias voltage.

An example of a commercially-available synthetic diamond detector is the PTW (Freiburg, Germany) microDiamond TN60019, which has a miniature active volume designed to reduce the volume averaging effects in small field dosimetry. The RSV of this detector is constituted by the diamond depletion region that encompasses the 1 μm thick diamond layer below a thin 1.1 mm radius aluminum contact to form a 0.004 mm^3 cylindrical active volume [45]. A schematic of the detector is shown in Figure 2–2, as provided by the manufacturer, and a micro CT projection image illustrating the internal components of the detector is presented in Figure 2–3.

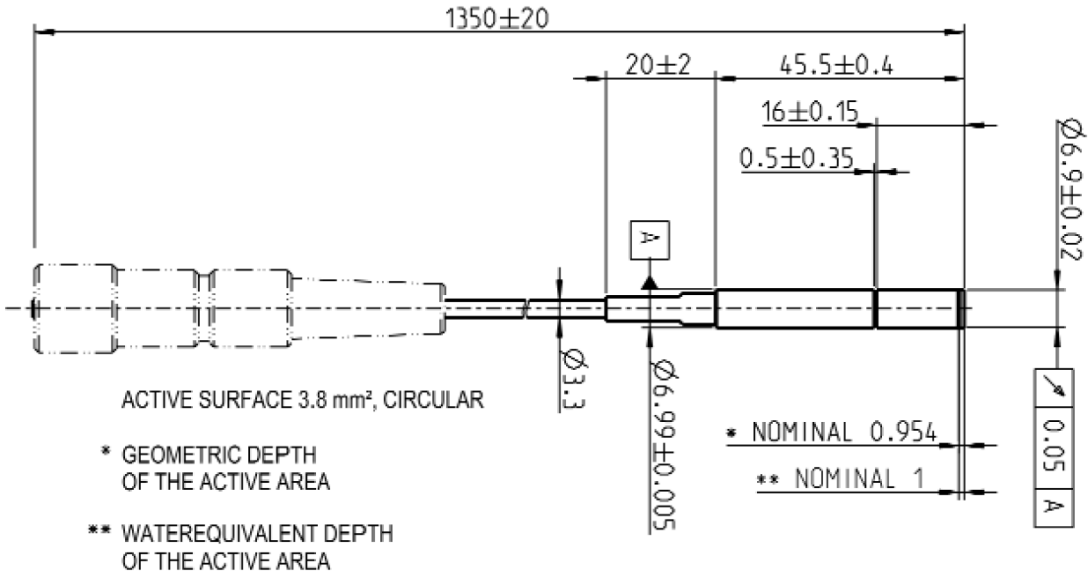

Figure 2–2 – PTW microDiamond TN60019 scheme (image taken from [40]).

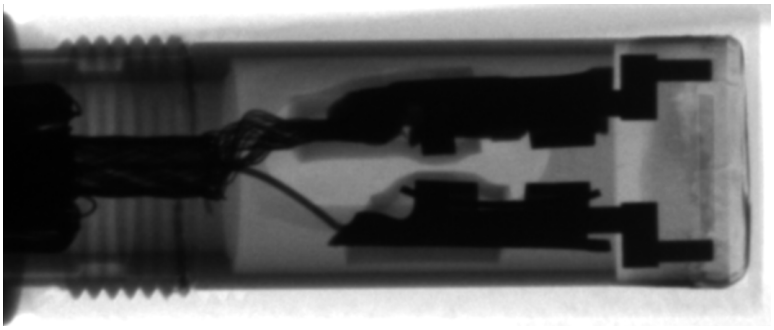

Figure 2–3 – Projection image from a micro CT taken from a PTW microDiamond TN60019 where the internal components are detailed. The image was acquired with a MEDISO NanoScan SdC at the McGill University Health Centre, using an x-ray tube setup of 35 kVp and 1 mAs.

In the image from the micro CT (Figure 2–3), the diamond plate can be observed embedded in the detector housing in between two aluminum pins that are joint to the plate connectors by thin cables not seen in the image [46].

Energy and Dose Rate Dependence

Diamond detectors have been proven to posses high dose and dose-rate linearity, as well as a low energy dependence in a wide range of photon energies from ^{60}Co to 25 MV [45, 38]. The low energy dependence is due to small variations in the water-to-diamond ratios of mass energy absorption coefficients and stopping powers in the indicated energy range. Dose-to-water to dose-to-diamond ratios are also nearly constant with depth in water despite energy spectrum changes, making them suitable for depth dose measurements in water phantoms. The low energy dependence of these detectors has also been explored in difficult-to-measure dose distributions around brachytherapy sources such as the ^{192}Ir [47], and in kilovoltage x-ray beams from 30 to 125 kVp. Deviations of less than 4 % were found in the energy range of 45 to 125 kVp [43, 45, 48], worsening to no more than 6 % for lower energies of 30 kVp [45]. Different studies found low dose rate dependence of the detector, with negligible variations in the range $1 - 700$ Gy s^{-1} [45] and deviations below 0.3 % in the dose rate range of 0.17 to 5.45 Gy min^{-1} [49]. To put these values in context, the reported effective energy of the INTRABEAM, at 10 mm depth in water, is 20.4 keV [31], and reported dose rates delivered by the source are 13.93 Gy/min [12] (and $\sim$20 Gy/min [33]) at 5 mm depth in water, 2.674 Gy/min [12] (and $\sim$4 Gy/min [33]) at 10 mm, and decrease to 0.4730 Gy/min at 20 mm and 0.1629 Gy/min at 30 mm [12].

The aforementioned characteristics make of the synthetic diamond a good candidate for the dosimetry of the INTRABEAM system.

2.3 Kilovoltage Photon Dosimetry Protocols

2.3.1 Absolute, Reference and Relative Dosimetry

To assure accurate determination of absorbed dose or other radiation quantity using a radiation dosimeter, a set of quality requirements have been established, and intercomparisons with previously calibrated detectors or calibration factors relative to measurements at primary standards laboratories are generally required. Depending on the level of accuracy of the measurement and the intercomparisons required, dosimetry procedures can be classified as follows:

- *Absolute dosimetry*: Based on measurements performed with instruments of the highest metrological quality, which allow the direct determination of the radiation quantity of interest from its definition, and that do not require a calibration from other reference systems. These measurements are performed at a *primary standards laboratory*, and the instruments used are known as *primary measurement standards* [50].

  Absolute dosimetry of kilovoltage x-ray beams is usually performed using a free-air ionization chamber to determine the air kerma in air from the energy transferred to the mass of air in the ion chamber RSV [38].

- *Reference dosimetry*: In this case, a radiation dosimeter that carries a calibration coefficient traceable to a primary standards laboratory is used to determine the radiation quantity of interest at the user's facility or clinic. The dosimeters used in these protocols are called reference (or transfer) detectors. Several correction factors might be required to account for differences in the measurement conditions at the standard laboratory to those at the clinic.

Reference detectors for low energy x-rays are typically soft x-ray ionization chambers, and the quantity of interest is usually the air kerma. Examples of the most common reference dosimetry protocols for kilovoltage x-ray beams include the AAPM TG-61 [6], IAEA TRS-398 [42], IPEMB [51] and addendum [52], DIN 6809 [53], DIN 6809-5 [54], and NCS-10 [55].

- *Relative dosimetry*: These procedures are employed to determine radiation quantities outside of the reference conditions used in reference dosimetry. Therefore, relative dosimetry is important in the studies of dose distributions. A common example is the determination of dose distributions in water around brachytherapy sources, in which it is necessary to obtain the dose in points other than that of the reference from the radioactive source for which the calibration factor has been provided. In this case, the dose to water is obtained by applying ratios and correction factors. The most common dosimetry protocol developed for reference and relative dosimetry of brachytherapy sources is the AAPM TG-43 [35] and its update [36], which will be discussed later in this chapter.

2.3.2 Reference Dosimetry - AAPM TG-61 Protocol

One of the most widely used dosimetry protocols for the reference dosimetry of kilovoltage photon beams is the AAPM TG-61 [6], which covers the range of superficial and orthovoltage x-ray (40 kV $\leq$ tube potential $\leq$ 300 kV) units that are used for treatment of superficial lesions like skin cancer, keloids, and others. This protocol establishes as beam quality specifiers the peak tube potential (kVp) in addition to the beam HVL.

The low-energy part of the TG-61 protocol is an air kerma based protocol in which the quantity of interest is determined with a soft x-ray ionization chamber as reference dosimeter according to

$$K_{\mathrm{air}} = N_K \, M, \tag{2.17}$$

where the calibration factor N_K, provided by a primary standards, is used to obtain the air kerma from the measured current, M, after being corrected for the chamber influence quantities described in Section 2.2.1.

The absorbed dose to water per monitor unit at the surface of a water phantom can be determined from the in-air method described in the TG-61 protocol according to

$$D_{w,\,z=0} = M \, N_K \, B_w \, P_{\mathrm{stem,\,air}} \left[\left(\frac{\bar{\mu}_{\mathrm{en}}}{\rho} \right)_{\mathrm{air}}^{w} \right]_{\mathrm{air}}, \tag{2.18}$$

where M and N_K have been defined above; the backscatter factor B_w accounts for the effect of the phantom scatter; $P_{\mathrm{stem,\,air}}$ refers to the chamber stem correction factor; $[(\bar{\mu}_{\mathrm{en}} \,/\, \rho)^{w}_{\mathrm{air}}]_{\mathrm{air}}$ is the ratio water-to-air of the mean mass energy-absorption coefficient in free air. Assuming that the field size of the measurement is similar to that of the ion chamber calibration, then the in-air chamber stem correction factor can be taken as unity ($P_{\mathrm{stem,\,air}} = 1$). The B_w and $[(\bar{\mu}_{\mathrm{en}} \,/\, \rho)^{w}_{\mathrm{air}}]_{\mathrm{air}}$ factors are obtained from tables. In the TG-61 protocol, tables for B_w are given as a function of source to surface distance (SSD), field size, and HVL. Values are given for $[(\bar{\mu}_{\mathrm{en}} \,/\, \rho)^{w}_{\mathrm{air}}]_{\mathrm{air}}$ factor as a function of the specified first HVL.

For medium-energy x-rays, the protocol provides an alternative method to determine the absorbed dose at 2 cm depth in water according to

$$D_{w,\,z=2\,cm} = M\,N_K\,B_w\,P_{Q,\,cham}\,P_{\text{sheath}}\left[\left(\frac{\bar{\mu}_{\text{en}}}{\rho}\right)^{w}_{\text{air}}\right]_{\text{water}}, \tag{2.19}$$

where the factor $P_{Q,\,cham}$ accounts for the overall contribution to the measurement due to the chamber stem and the water displacement by the presence of the chamber. P_{sheath} corrects for the waterproofing cap, (if present) and the $[(\bar{\mu}_{\text{en}}\,/\,\rho)^{w}_{\text{air}}]_{\text{water}}$ factor is now established at 2 cm in water.

2.3.3 Relative Dosimetry - AAPM TG-43 Protocol

The AAPM TG-43 protocol [35] and its update [36] provide a procedure to determine absorbed dose distributions in water around photon-emitting brachytherapy sources.

In contrast to the TG-61 which is air kerma based, the TG-43 is based on air kerma strength and a conversion procedure to absorbed dose to water. In the TG-43, reference dosimetry is performed with a re-entrant well chamber and its corresponding calibration coefficient provided by a national standards laboratory. The *air kerma strength* S_K is the standard quantity used as reference for brachytherapy sources calibration, and determines the air kerma rate measured at a specified distance according to

$$S_K = \dot{K}_\delta(d)\,d^2, \tag{2.20}$$

where $\dot{K}$ is the air kerma rate measured *in vacuo* at the reference distance d and due to the contribution of only photons of energy greater than δ. This relation gives

the air kerma strength units of μGy m^2 h^{-1}, or its equivalent cGy cm^2 h^{-1}, which is denoted by U.

The TG-43 protocol is based on the reference coordinate system shown in Figure 2–4. The reference point in TG-43 is taken at $r_0 = 1$ cm and $\theta = 90°$ relative to the source longitudinal axis.

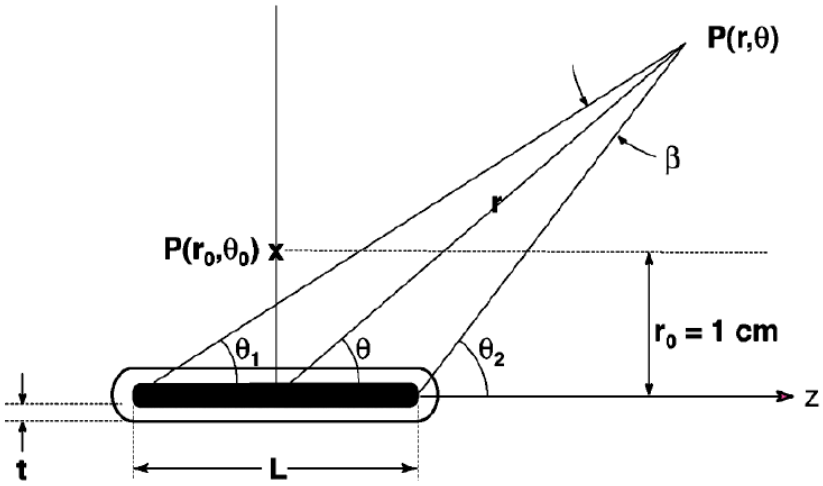

Figure 2–4 – Reference coordinate system for the TG-43 dosimetry protocol (image taken from [36].)

For the general bi-dimensional (2D) formalism, which apply for cylindrically symmetric sources using the line-source approximation, the absorbed dose rate at any point $P(r, \theta)$ in water can be determined from the dose rate at a reference point $P(r_0, \theta_0)$ according to

$$\dot{D}(r, \theta) = S_K \, \Lambda \, \frac{G_{\mathrm{L}}(r, \theta)}{G_{\mathrm{L}}(r_0, \theta_0)} \, g_{\mathrm{L}}(r) \, F(r, \theta), \tag{2.21}$$

where the subscript L indicates the use of the line-source model, the *dose-rate constant*, $\Lambda = \dot{D}(r_0, \theta_0) \,/\, S_K$, is a source-specific parameter such that the product $S_K \, \Lambda$

provides the dose rate at $P(r_0, \theta_0)$, and the accompanying functions correct for geometry, scattering and attenuation in water in the 2D distribution. Specifically, the *geometry function*, $G_{\mathrm{L}}(r, \theta)$ provides an effective inverse square-law correction, neglecting all scattering and attenuation effects. The *radial dose function*, $g_{\mathrm{L}}(r)$, corrects for the dose fall-off in the transverse plane ($\theta = 90°$) due to scattering and attenuation effects, thus neglecting the geometry contribution. The function is obtained as

$$g_{\mathrm{X}}(r) = \frac{\dot{D}(r, \theta_0)}{\dot{D}(r_0, \theta_0)} \frac{G_{\mathrm{X}}(r_0, \theta)}{G_{\mathrm{X}}(r, \theta_0)}, \tag{2.22}$$

where the subscript "X" indicates that whether the line-source, "L", or point-source, "P", approximations can be used. $g_{\mathrm{X}}(r)$ equals unity at $r_0 = 1$ cm. The *anisotropy function*, $F(r, \theta)$, accounts for dose rate variations at any polar angle position relative to the transverse plane, and is defined as

$$F(r, \theta) = \frac{\dot{D}(r, \theta)}{\dot{D}(r, \theta_0)} \frac{G_{\mathrm{L}}(r, \theta_0)}{G_{\mathrm{L}}(r, \theta)}. \tag{2.23}$$

The point-source approximation can be used when the active length of the source, L, is small and has a negligible effect on the dose calculations. For these situations, the geometry function corresponds to the inverse-square law, $G_{\mathrm{P}}(r, \theta) = r^{-2}$, and Eq. 2.21 can be expressed as

$$\dot{D}(r, \theta) = S_K \, \Lambda \left(\frac{r_0}{r} \right)^2 g_{\mathrm{P}}(r) \, F(r, \theta). \tag{2.24}$$

2.4 INTRABEAM Dosimetry

2.4.1 Source Calibration

The INTRABEAM system is calibrated by the manufacturer (Carl Zeiss Meditec AG, Jena, Germany) using a water phantom and a PTW 23342 soft x-ray ionization chamber, and a calibration depth dose curve is provided for each INTRABEAM source [31]. The methodology is exposure-based and uses a calibration coefficient, N_s, from a free-air chamber primary standard. With this method, the rate of absorbed dose at different depths in water is determined from current measurements as

$$\dot{D}_w(z)\left[\frac{Gy}{min}\right] = I_{T,P}(z)[A]\, N_s\left[\frac{R}{C}\right] k_Q\, f\left[\frac{Gy}{R}\right] 60\left[\frac{s}{min}\right], \tag{2.25}$$

where $I_{T,P}(z)$ has been corrected for temperature and pressure to the reference conditions, k_Q corrects for beam quality differences from that during calibration, and the roentgen-to-gray conversion factor, f, is tabulated for different photon energies. For a reference energy value of 20 keV for the INTRABEAM, $f = 8.81$ mGy R^{-1} and $k_Q = 1.000$.

After the calibration depth dose curve has been obtained, the isotropy is verified as described in Section 1.3.2, and applicator transfer functions are obtained. These transfer functions are calculated as the quotient of the depth doses measured with and without the applicator, and are also provided by the manufacturer.

2.4.2 Depth Dose Verification - Zeiss Method

In order to verify the calibration tables provided by the manufacturer, a water phantom for independent measurements is provided [56]. This Zeiss Water Phantom, shown in Figure 2–5, includes two plastic holders to insert a PTW 34013 soft x-ray

ionization chamber, which is not waterproof. The holder besides the source needle is used for isotropy measurements and is use in conjunction with the rotary stage shown in the figure. The holder located below the source is used for depth dose measurements. In the last case, the ion chamber is inserted and the INTRABEAM source is moved up in the stage, using the positioning unit screws also indicated in the figure. Usual depths for depth dose measurements, relative to the source tip, range from 3 mm to 45 mm in 0.5 mm steps. The precision of the positioning unit is of 0.01 mm.

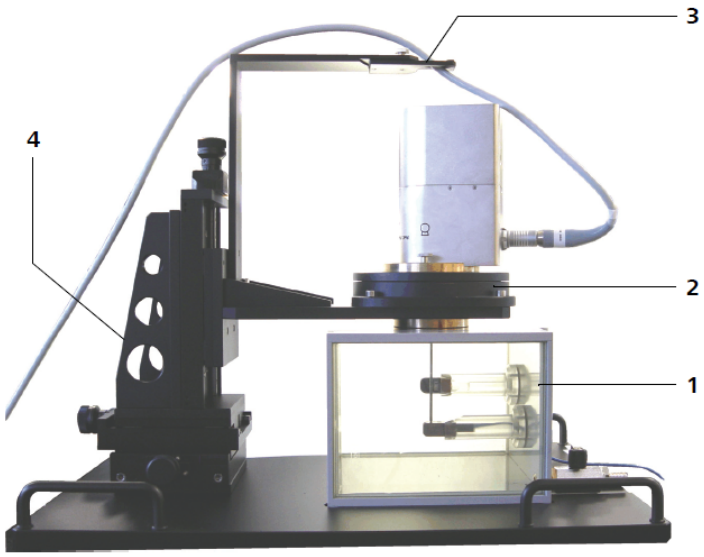

Figure 2–5 – Zeiss Water Phantom indicating the water tank (1), the rotary stage (2), a cable holder (3), and the positioning unit (4) (image taken from [56]).

The verification method described here is called the *Zeiss method* for the remainder of this work, and makes use of the air kerma based calibrated chamber PTW 34013. The charge readings are then converted to dose to water using the

Zeiss method for the water tank as depicted by

$$D_w^{Zeiss}(z) = M(z)\, N_K\, k_Q\, k_{\mathrm{K_a \to D_W}}, \tag{2.26}$$

where $M(z)$ are the average charge measurements at different depths z, corrected by temperature and pressure, N_K is the air kerma calibration coefficient of the chamber, k_Q is the correction factor for beam quality, and $k_{\mathrm{K_a \to D_W}}$ is an air kerma to dose to water correction factor provided by Zeiss.

In order to compare the measurements with the calibration depth dose curves, the obtained *Zeiss dose* must be multiplied by an additional factor, $f'(z)$, that, according to the Zeiss dosimetry protocol, corrects for differences in the ionization chamber models (PTW 23342 and PTW 34013), differences in ionization chamber holders, and use of two different algorithms to calculate the dose, one using a exposure-to-dose conversion factor and the other an air kerma-to-dose conversion factor. Since the exposure-based model used for the calibration of the INTRABEAM is the same that was employed during the TARGIT-A clinical trial, the obtained dose with the correction factor is called the *TARGIT dose* and is calculated by the *TARGIT method*

$$D_w^{TARGIT}(z) = f'(z)\, D_w^{Zeiss}(z). \tag{2.27}$$

2.4.3 Depth Dose Verification - C_Q Method

In contrast to the Zeiss method, Watson *et al* [33] showed that the conversion from air kerma to dose-to-water, $k_{\mathrm{K_a \to D_W}}$, is energy dependent and conversion factors vary with depth in water. In addition, an inconsistency in the Zeiss method was identified, since it is not clear which value represents the true physical absorbed

dose, the Zeiss dose, or the TARGIT dose, or none of them. Then, they proposed a new formalism in which a depth dependent factor, $C_Q(z)$, which is MC calculated, is used to determine the dose to water according to

$$D_w^{C_Q}(z) = M(z)\, N_K\, C_Q(z). \tag{2.28}$$

This formalism will be referred to as the C_Q method in the remainder of this work.

2.4.4 Relative Dosimetry

Due to the applications and dosimetric similarities of the INTRABEAM with brachytherapy sources, the system can be studied as an electronic brachytherapy source, as introduced in Section 1.2.4. As such, the relative dosimetry of the INTRABEAM can be assessed using the AAPM TG-43 dosimetry protocol. However, this protocol has been used only for the Xoft Accent electronic brachytherapy source but not for the INTRABEAM. In this section, the procedure and adaptation of the TG-43 formalism for the Xoft electronic brachytherapy source is summarized.

In the protocol for the Xoft source by Rivard *et al* [18], the effective length is small, and then, Eq. 2.24 for the 2D formalism with a point-source approximation was used. In this formalism, the calibration based on the air kerma strength, S_K, obtained at a primary standards laboratory, required an *in-vacuo* conversion of the air kerma rate by applying corrections for scatter and attenuation in air and in the surrounding media. This procedure, however, was not appropriate for electronic brachytherapy sources, since the scatter and attenuation corrections were significant. For example, the attenuation correction for the Xoft source was higher than 25% [57].

For this reason, a modified formalism using the air kerma rate measured in air, $\dot{K}_{\text{air}}$, instead of air kerma strength, was developed at the National Institute of Standards and Technology (NIST). With this modification, the dose rate is calculated according to

$$\dot{D}_i(r,\theta) = \dot{K}_{50\text{cm}}\, \chi_i(1\,\text{cm},\, \pi/2)\, G_{\text{P}}(r,\theta)\, g_i(r)\, F_i(r,\theta), \tag{2.29}$$

where the subscript i makes reference to the dose rate calculation for a source applicator i, $\dot{K}_{50\text{cm}}$ is the air kerma rate measured in air at 50 cm from the source, with traceability to NIST, $\chi_i(1\,\text{cm},\, \pi/2)$ is the *dose-rate conversion coefficient* at the reference point $r_0 = 1$ cm, $\theta_0 = 90°$, $G_{\text{P}}(r,\theta) = r^{-2}$ is the geometry function with point source approximation, and $g_i(r)$ and $F_i(r,\theta)$ are the radial dose function and the 2D anisotropy function for the applicator i, respectively.

Note that, as stated in Section 1.4, the dose-rate conversion coefficients, $\chi_i(1\,\text{cm},\, \pi/2)$ in Eq. 2.29, were not determined in this thesis, since air kerma rates at 50 cm for the INTRABEAM are still not provided by a standards laboratory.

2.5 Monte Carlo Techniques

2.5.1 Basics of Monte Carlo Simulations

In radiation therapy situations are found complex geometries, wide range of interaction particles and physics phenomena, as well as a variety of interacting media, compositions and interfaces. For this reason, an analytical model for a particular situation, able to accurately reproduce the radiation propagation in media and find the distributions of a radiation quantity of interest, can be impractical or impossible to develop. The advent of Monte Carlo (MC) techniques aimed to solve the issue by simulating the interaction of millions of particles with the geometry of interest using

probability distributions. With MC, each particle initiates the simulation process with an energy and direction chosen in a pseudo random manner, based on probability distributions for the specific source. Particles will then move a certain distance, chosen also from a probability distribution, and will interact with the media by scattering (with a new direction and energy), depositing energy, and/or ejecting a new secondary particle. The process will continue until the energy of the particle falls below a defined threshold (and the particle is absorbed) or until the particle leaves the volume of interest. The quantities of interest are then obtained by averaging over the scored value resulting from many of these particle interactions [58, 38]. The uncertainties on the estimation of the quantity of interest will decrease with the number of particle histories simulated, N, and is given by the standard deviation of its mean value, σ, which is generally inversely proportional to $\sqrt{N}$.

The high number of particle histories required are usually associated with a high demand on computation time and resources. In order to reduce the computation times, the user can make use of appropriate *variance reduction techniques*.

2.5.2 Variance Reduction Techniques

Different methods that can reduce the computation times of a simulation without affecting the accuracy of the physics are called variance reduction techniques [38]. Examples of variance reduction techniques employed in the present work are described below.

- *Photon splitting*: A primary photon is split into multiple photons by a factor n_s. The statistical weight of the split photons is $1/n_s$, and their interaction points coincide at uniformly distributed locations along the direction of the

primary photon. Photon splitting can be used, for example, to increase the number of bremsstrahlung photons generated at the anode of an x-ray tube.

- *Russian Roulette*: When an event is forced to occur, as in the case of photon splitting, statistical weight corrections must be applied. One correction method is the Russian Roulette, in which particles are selectively eliminated by terminating its transport using a specific survival probability w. Surviving particles will have a statistical weight increased by a factor $1/w$. A special case of the technique is called range-based Russian roulette, in which electrons that have not enough energy to reach a volume of interest will be terminated in a random way using Russian roulette to reduce computation times.
- *Photon cross section enhancement*: The technique increases the photon cross sections in specified regions with the subsequent weighting factor corrections to avoid statistical bias. The technique can be used to increase the probabilities of photon interactions in materials near the RSV of a dosimeter.
- *Intermediate Phase Space Storage*: The technique consists on using an artificial volume surrounding a region of interest for which the dosimetric quantity wants to be determined, for example, the volume enclosing all possible positions of an ionization chamber in the acquisition of depth dose curves and profiles in a water phantom. The information of particles entering this volume is stored in a file called *phase space*, and will be used later as a virtual source for small variations on the geometry, as in the case of ion chamber movements along the dose profiles, avoiding the need of recalculating the particle transport in the entire geometry [59].

- *Fluence-based estimators*: These are not strictly VRTs but help improving the efficiency of MC calculations. In this technique, all the particles going through a volume element contribute to the quantity of interest, even though the particles do not interact within the scoring volume. A *tracklength estimator* is an example of this group, in which all photons traversing the volume of interest contribute to the kerma estimate, reducing the associated variance [38, 60].

In addition to the variance reduction techniques, approximations can be used to reduce the simulation times. Techniques that use approximations are called *speed-up techniques* [38]. An example of them is to increase the energy cut-offs for absorption of photons and electrons [38].

2.5.3 EGSnrc Particle Transport Code

Numerous systems and codes have been developed to perform Monte Carlo calculations in radiation dosimetry applications, including Geant4 [61], PENELOPE [62], MCNP [63] and EGSnrc [64].

The EGSnrc code system was used for the simulation of INTRABEAM dosimetry since it allows for an easy implementation of a wide variety of geometries, particles and particle energies in the energy range of interest. With EGSnrc, electrons and photons can be transported through any element, compound, or mixture, with energies that can go down to 1 keV [64]. A complete set of physics processes can be included in the simulations, namely bremsstrahlung production, using NIST cross sections; positron annihilation (though it is of low importance in the energy range of interest); multiple scattering of charged particles using the Molière theory [65];

Møller and Bhabha scattering for electron-electron and positron-electron interactions, respectively; continuous energy losses for charged particles; pair production (not relevant for INTRABEAM dosimetry); Compton scattering using Klein-Nishina or bound Compton using the impulse approximation (for low energy photons); coherent (Rayleigh scattering); photoelectric effect; atomic relaxations with fluorescence emissions; and electron impact ionization.

Examples of EGSnrc applications used in this work include the egs_chamber [59] and egs_brachy [66] user codes, which employ the library egs++ [67], based on c++ language, which together allow the simulation of different radiation detectors and brachytherapy sources and models, allowing the use of the variance reduction techniques mentioned in Section 2.5.2, and a dosimetric evaluation of the INTRABEAM system.

Chapter 3
Materials and Methods

In this chapter, the Monte Carlo model of the INTRABEAM source and simulation specifications to obtain the TG-43 parameters are described in detail. In addition, an overview of the materials and methodology employed for the experimental dosimetry and simulation validations with two different radiation dosimeters are discussed.

3.1 Monte Carlo Simulations

3.1.1 INTRABEAM Source Geometry

For a simulation of the INTRABEAM source for the purpose of quantifying TG-43-type dosimetry functions with the goal of describing accurate dose distributions around the source, the geometry must be described with much more detail than the basics provided in Section 1.3.1. Electrons produced in the electron gun are accelerated with a Gaussian distribution of energy with mean of 50 keV and full width at half maximum (FWHM) of 5 keV [24]. The electrons are then transported in vacuum towards the tip of the 10 cm long, 3.2 mm outer diameter probe where approximately 50 kVp x-rays are produced by bremsstrahlung and fluorescence in a 0.5 μm thick gold target that covers the inner surface of the hemispherical end of the source [22, 23]. The metallic probe wall is surrounded by thin biocompatible [68] layers and its 1.6 cm distal part is substituted by a beryllium x-ray window [23]. The materials and composition of the INTRABEAM source were modeled according

to the specifications provided by Nwankwo *et al* (2013) [68] as presented in Table 3–1, and a geometry reconstruction used in the simulations is shown in Figure 3–1. The geometry and Monte Carlo model of the source up to this point were previously developed and provided by Watson *et al* [33, 34], however, variations were included in the source definitions for the present work. The electron beam is internally deflected in the evacuated needle using a magnetic beam deflector, in a way that the target can be described as 'ring' shaped, producing a nearly isotropic dose distribution around the probe tip [24, 25, 26]. This effect, together with the Gaussian distribution in energy, were added to the source model in this work.

Table 3–1 – INTRABEAM source materials and composition according to Nwankwo *et al* (2012) (Table edited from [33]).

Materials		Thickness [μm]
Target	Au	1.0
Body	Be	500
Biocompatible layers	NiO	2.5
	Ni	2.5
	CrN	2.5

3.1.2 Particle Source

As mentioned above, accurate simulations of the source probe must include a description of the effective target shape due to internal electron beam deflections. According to the manufacturer, the internal beam deflection is induced to improve the polar symmetry of the dose distribution around the source. This work follows the results of the investigation by Clausen *et al* (2012) [24], who found that the incoming electrons hit the gold target in the shape of two concentric rings of radii 0.6 to 0.7 mm and 0.7 to 0.8 mm, with weighting factors of 1.05 and 1.55, respectively, with a

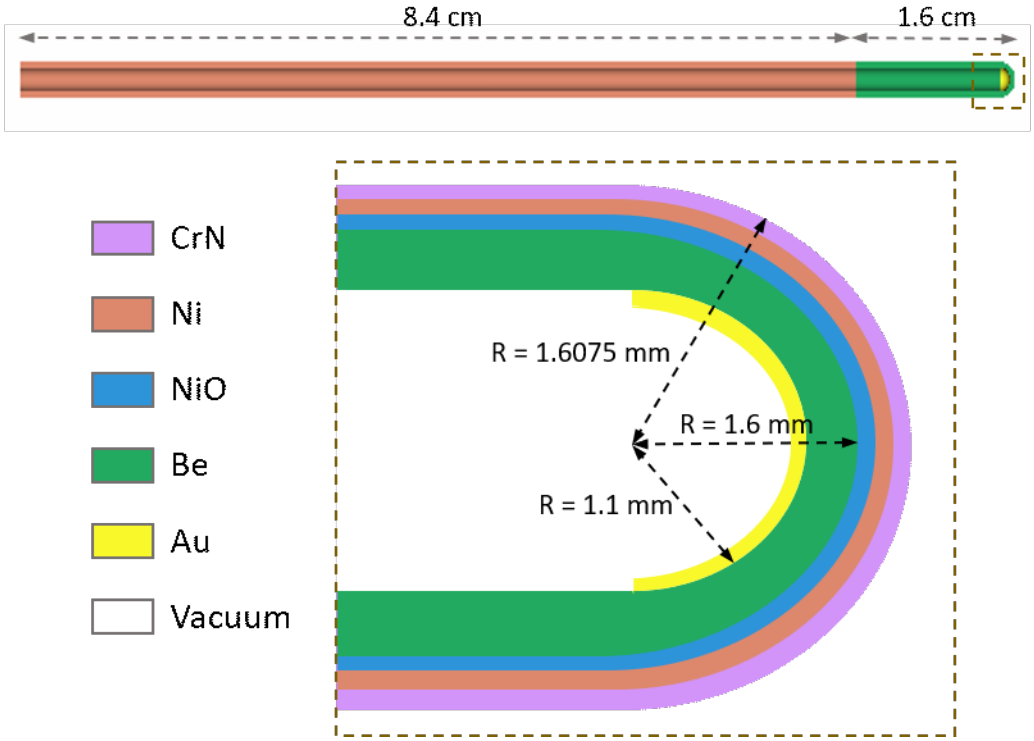

Figure 3–1 – Reconstruction of the INTRABEAM source geometry used for the MC simulations. The inset below (not to scale) shows the zoomed cross sectional view of the source tip with the beryllium window, the gold target and the biocompatible layers materials and dimensions, as used in this work (material specification adapted from Nwankwo *et al* (2013) [68]).

Gaussian distribution in energy with mean at 50 keV and FWHM of 5 keV. This particle source was constructed in egs_brachy as a combination of two collimated sources generating hollow cones with apex at the proximal end of the probe, and projecting the required rings 10 cm downstream on the base of the gold target, as illustrated in Figure 3–2. The effect in the dose distribution of the deflected electron beam of the particle source is analyzed by comparing the results against the simulation of a parallel source of mono-energetic 50 keV electrons directed towards

the source tip and coming from a 2.2 mm diameter circle placed at the base of the gold target.

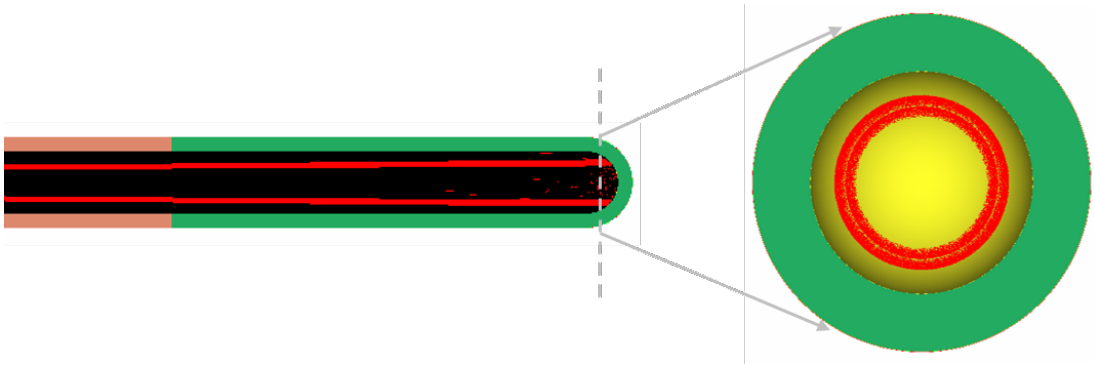

Figure 3–2 – Rendering of the source model showing the internal electron particle source as composed by two individual rings with radii 0.6 to 0.7 mm and 0.7 to 0.8 mm when projected to the gold target.

3.1.3 Radiation Transport Parameters

The dose distribution in water around the source was determined with Monte Carlo (MC) calculations using egs_brachy (v2017.09.15) [66]. For the low-energy range of photons usually observed in brachytherapy, egs_brachy allows rapid dose calculations by approximating dose to electronic kerma obtained via a tracklength estimator, and developed new dedicated variance reduction techniques for electronic brachytherapy sources.

In this study, simulations were run from the interactions of the electron beam striking the gold target using the transport parameters predefined in an EGSnrc input file and the different materials and geometry provided by the INTRABEAM manufacturer (Carl Zeiss, Germany). All the EGSnrc physics processes for low-energy photons were included in our simulations, as for example Rayleigh scattering,

bound Compton scattering, photoelectric absorption and atomic relaxations for K, L, M and N shells. Penelope libraries were used for electron impact ionization. The photon and bremsstrahlung cross sections were modeled using the XCOM [69] and NRC databases, respectively. The transport cut-off energy for photons (PCUT) was set at 1 keV, and for electrons (ECUT) inside the source was set at 512 keV (1 keV kinetic energy). Electrons were not transported outside the source (ECUT = 1 MeV) because dose was approximated as electronic kerma, and was calculated using the mass energy absorption coefficients for water (ρ = 1.0 g cm^{-3}) provided by egs_brachy in a data file. Cross section data for the materials in the geometry was generated covering the energy range from 1 keV to 1.5 MeV, assuring accurate transport modelling of the simulated low-energy photons and electrons. Variance reduction techniques used include bremsstrahlung cross section enhancement in the gold target by a factor of 50, uniform bremsstrahlung splitting with a factor of 100, and the associated statistical weights corrections using Russian roulette.

For dose calculations with radiation detectors such as an ionization chamber and a diamond detector, the egs_chamber user code was also employed, applying all the variance reduction techniques described in Section 2.5.2.

3.1.4 TG-43 Parameters

The specific dimensions of the INTRABEAM source are proprietary restricted but the gold target can be modelled with a very small effective length ($L_{\text{eff}} < 1$ mm). Therefore, the 2D formalism will be followed, as proposed by Rivard *et al* [18] for the Xoft electronic brachytherapy source, with a point-source approximation used to describe the geometry function, $G_{\text{p}}(r, \theta) = 1/r^2$, and radial dose function, $g_{\text{p}}(r)$,

but using the 2D formalism to account for polar anisotropy, $F(r,\theta)$, close to the source probe. According to the specifications of the INTRABEAM source geometry, azimuthal symmetry around the source long axis is assumed.

The TG-43 parameters $g_{\mathrm{p}}(r)$ and $F(r,\theta)$ of Eq.2.24 were determined with MC calculations. For this, the coordinate system origin was located at the source tip, and $\theta = 0\,^{\circ}$ points towards the distal part of the source as illustrated in Figure 3–3.

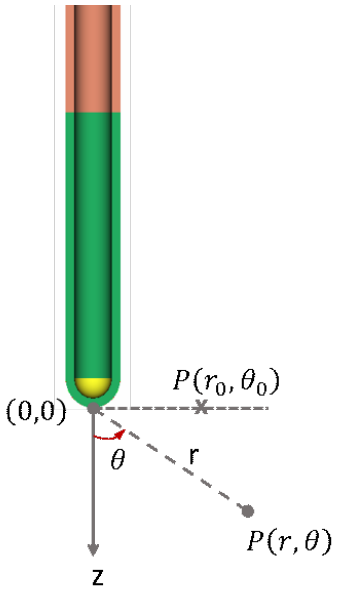

Figure 3–3 – Reference coordinate system used for determining the TG-43 parameters for the INTRABEAM source.

Dose rates were scored in a set of annular bins centered at the source longitudinal axis covering the region z = [-5, 5] cm and r = [0, 5] cm in 0.04 cm intervals in both, the longitudinal and radial, directions, as illustrated in Figure 3–4. Although TPSs require data in more extended volumes, points located outside the chosen region lead to dose rates too low to measure reproducibly and these also require considerably

longer computing time to reduce uncertainties to acceptable values. Hence, this volume was chosen as a representative volume, since most of the dose delivery occurs near the source, and the MC model can be accurately validated in this region. The scoring volume composition consisted of liquid water of mass density 1.0 g cm^{-3} and atomic composition 2:1 for H:O, and was immersed in a bigger spherical phantom of radius 20 cm and the same water composition to assure full scattering conditions in the scoring volume [18, 70]. The water phantom and scoring volume were centered at the source tip. In order to obtain sufficient statistics, $3 \cdot 10^9$ histories were run resulting in k = 1 statistical uncertainties in the range 0.1% to 0.5% over the source longitudinal axis, at 1 to 5 cm from the source tip.

The dose at voxels in water partially overlapped with the source surface was corrected to reduce *partial volume effects*. This effect occurs because there is no energy deposition scored in the fraction of the voxels inside the source, but the total voxel volume is included in the calculation of absorbed dose. In this case, the scored energy, E, in the phantom portion of the voxel is wrongly divided by the total voxel volume. To compensate for this effect, the dose in a voxel of volume V and media density ρ was estimated as

$$D = \frac{E}{p\,V\rho}, \tag{3.1}$$

where $p\,\epsilon\,[0,\,1]$ is the partial volume proportion located outside the source [24]. The partial volume p is precalculated by subdividing each voxel in 8000 subvoxels and then randomly determining how many of this subvoxels are inside and how many outside the source, and the results are scored for each voxel in a file that will be used

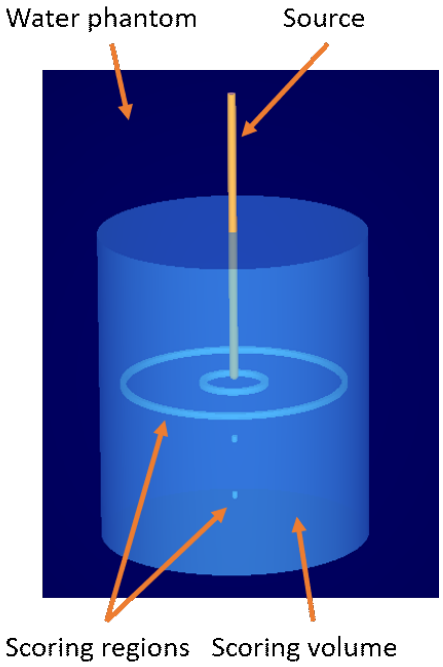

Figure 3–4 – Representation of some of the annular scoring volumes centered at the source longitudinal axis and contained in a bigger water phantom to assure full scattering conditions.

during the dose calculations. This process is performed once before submitting the jobs to a computer cluster for dose calculations.

In addition to the bare probe dose distributions, MC simulations were performed to get depth dose curves using the INTRABEAM spherical applicators. Schemes of the simulated applicator geometries with their materials are shown in Figure 3–5 for a 4 cm and the smallest 1.5 cm diameters. The bulk material of the applicators is ULTEM (polyetherimide) [28] with a nominal mass density of 1.27 g/cm^3. The aluminium filter used for the smaller applicators from 1.5 to 3 cm diameter is also

shown. Detailed dimensions and material compositions were provided by the manufacturer. The same water phantom and annular scoring volumes as for the bare probe were used. The dose distribution was obtained outside the applicator volume and partial volume effects in voxels at the applicator surface were corrected using Eq. 3.1.

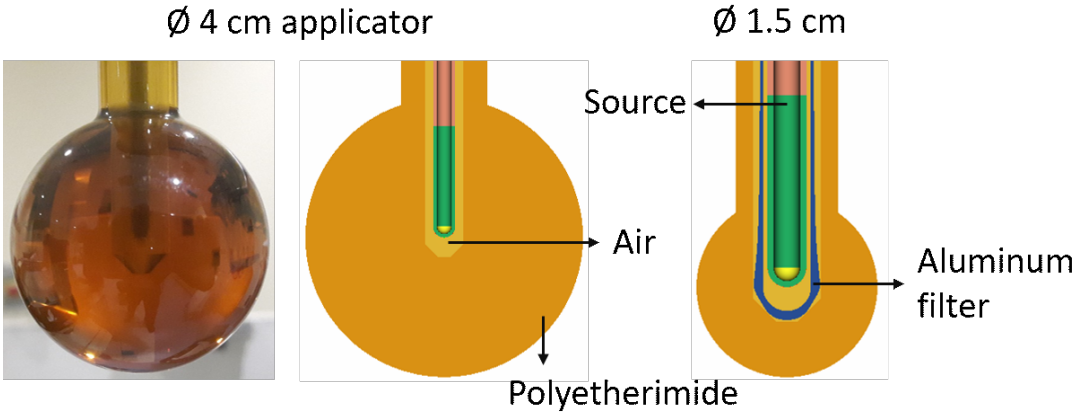

Figure 3–5 – Rendering of the spherical applicators models for the MC simulations. On the *left*, a picture of the 4 cm diameter applicator is compared with the simulation geometry. On the *right*, the 1.5 cm applicator rendering is presented with the aluminum filter included with sphere diameters from 1.5 to 3 cm.

Depth dose calculations with the MC model of the INTRABEAM bare probe and with applicators were validated against measurements in water and compared with the results of previous investigations [33].

MC simulations with a PTW TN60019 microDiamond detector were also run and evaluated. In order to account for energy dependence of the detector for the kilovoltage energy range of interest in water, simulations were run to calculate the dose to a small volume of water and to the diamond in the RSV of the microDiamond

detector, using the egs_chamber application of EGSnrc. A correction factor, C^{w}_{dia}, was obtained as the quotient of absorbed dose to water, D_w, to absorbed dose to diamond, D_{dia}, for each depth along the source axis at the range of interest, according to

$$C^{w}_{\mathrm{dia}}(z) = \frac{D_w(z)}{D_{\mathrm{dia}}(z)}. \tag{3.2}$$

This calculated factor was applied to measurements with the microDiamond in order to compare dose to water profiles from MC calculations and measurements.

3.2 Experimental Measurements

3.2.1 Measurements With Ionization Chamber

MC calculations were compared with measurements in water using a water phantom provided by the source manufacturer (Carl Zeiss, Germany)(shown in Figure 2–5), a PTW air kerma calibrated parallel-plate ionization chamber, model 34013 (scheme shown in Figure 2–1), connected to an electrometer PTW UNIDOS E, and an INTRABEAM source (S/N: 507366). The PTW 34013 ion chamber model is not waterproof, therefore, it is placed inside a water proofing holder attached inside the water tank. The setup for the measurements with the ion chamber is shown in Figure 3–6 for the bare probe (3–6a) and the 4 cm applicator (3–6b).

The measurements in the present work follow the methodology and recommendations described by Watson *et al* [33], based on the Zeiss water phantom manual [56]. Charge data was acquired from 60 s readings for each ionization chamber position, which was precisely shifted along the central axis of the source in a way that its effective point of measurement (EPOM) is moved from 2 to 50 mm depth from the source tip in steps ranging from 0.4 to 2.0 mm, with the smallest steps close

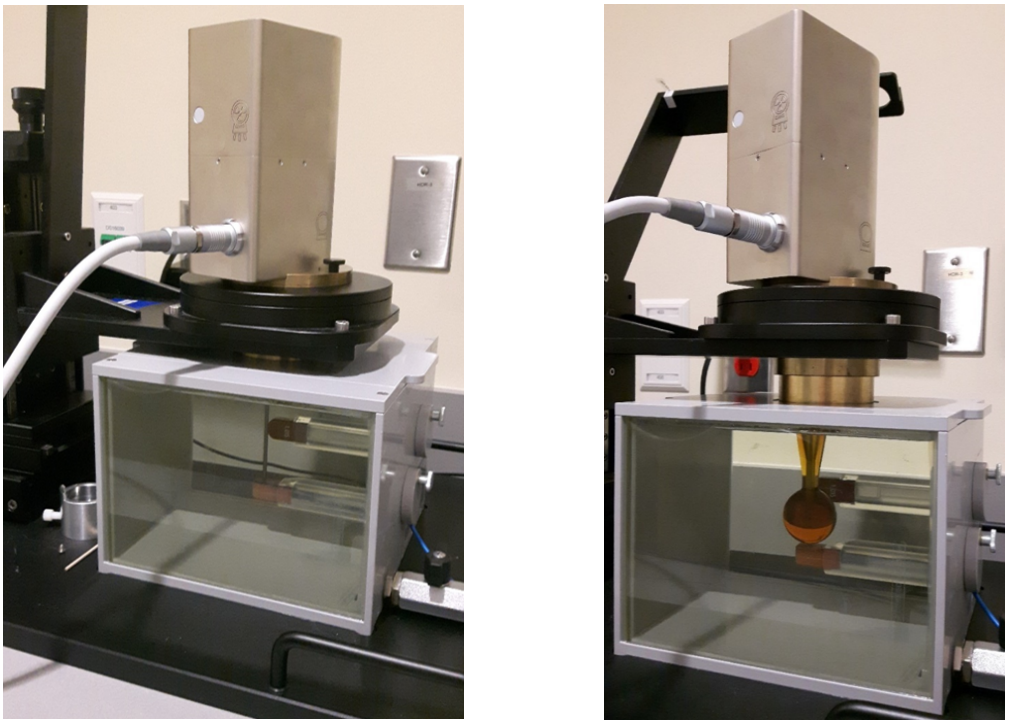

(a) Bare probe (b) 4 cm applicator

Figure 3–6 – Experimental setup for measurements with the PTW 34013 ionization chamber in a Zeiss Water Phantom. The ionization chamber is placed in the plastic holder below the bare probe (a) and below the 4 cm applicator (b).

to the tip where the dose gradients are steeper. Measurements were repeated three times in each chamber position and the mean values and standard deviations were determined.

In order to compare the measurements with the MC simulations, the charge readings were converted to dose to water using the Zeiss dosimetry protocol for the water tank as depicted by Eq. 2.26, and described in Section 2.4.2 with the corresponding charge measurement corrections for chamber influence quantities. Next, absorbed dose to water was obtained with the C_Q method according to Eq. 2.28

and the dosimetry protocol described in Section 2.4.3. The required C_Q factors for the range of depths evaluated in this study were provided by Watson *et al* from the results of their investigation with the same ionization chamber model [33, 34]. In addition, the results of the present investigation were compared with the measurements performed by Watson *et al* with a different INTRABEAM source (S/N: 507535) to assess possible systematic errors.

3.2.2 Measurements With Diamond Dosimeter

In the results from investigations of Watson *et al* [33] it was shown that high tolerances in the reported geometry specifications for plate separation and EPOM of the PTW 34013 ionization chamber lead to high uncertainties in the absorbed dose estimation, especially in zones of high dose gradients observed close to the INTRABEAM source. For this reason, an alternative detector with well defined and validated geometry, with a small RSV able to correct for volume averaging effects in high dose gradients, was required. In addition, measurements in the Zeiss Water Phantom with the PTW 34013 ion chamber were limited to a 1D profile along the source longitudinal axis, and a few isotropy measurements on its transverse plane at a specific distance from the source tip. These limitations suggest also the use of a different phantom with a more flexible setup for out-of-axis measurements required for 2D and 3D anisotropy verifications.

The measurement setup with a synthetic PTW TN60019 microDiamond and a Wellhöfer water tank with a 3D scanning system (WP700, version *V* 3.51.00, Wellhöfer Dosimetrie, Germany) is shown in Figure 3–7. With this system, the PTW microDiamond detector is connected through a triaxial cable to a Wellhöfer CU500E

Dual Processor Based Control Unit. An alternative electrometer, a Keithley model 6517A (Keithley Instruments, Inc., Cleveland, U.S.A.) was also employed for validations.

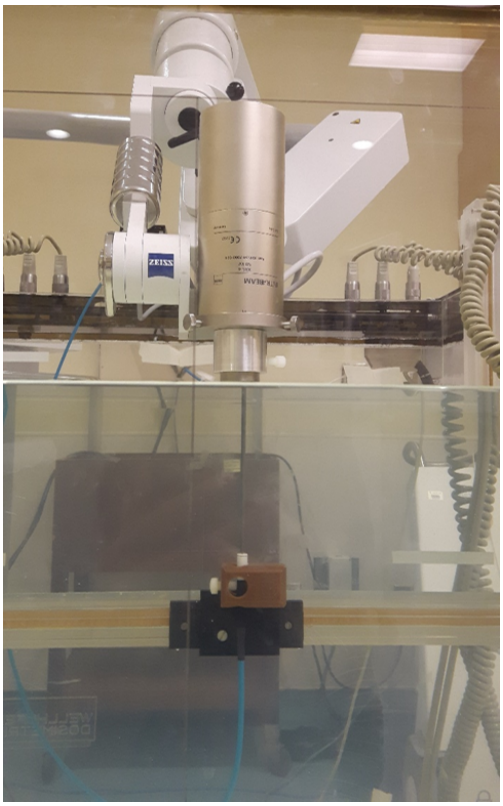

Figure 3–7 – Experimental setup for measurements with the PTW TN60019 microDiamond detector in a Wellhöfer water phantom. The ionization chamber is placed in a plastic holder attached to the Wellhöfer automated 3D scanning system (WP700, version *V* 3.51.00, Wellhöfer, Germany).

Measurements with the microDiamond were performed in 0.1 mm steps in the range from 0.2 to 5 cm depth in water from the source tip, along the source longitudinal axis. By default, the INTRABEAM system does not allow to operate the machine with the INTRABEAM arm without the use of any applicator, since that

is the safest way to be operated with a patient during IORT. In order to perform measurements with the bare probe, an in-house built accessory was constructed to bypass the INTRABEAM interlock system, as can be seen attached to the distal part of the arm in Figure 3–7. The obtained depth dose curves with the microDiamond were converted to dose to water distributions using the correction factor of Eq. 3.2.

Chapter 4
Results and Discussion

4.1 MC Model Validation

4.1.1 Measurements With Ionization Chamber

The results of the MC simulated depth doses for the INTRABEAM bare probe in a water phantom, normalized to 1.0 at a depth of 1 cm from the source tip, are shown in Figures 4–1 and 4–2, along with the measurements performed in a Zeiss Water Phantom using the PTW 34013 ionization chamber and an INTRABEAM source (denoted as *Source* 1), and a second set of measurements obtained by Watson *et al* (2017) [33] using a different INTRABEAM source (denoted as *Source* 2). The plotted measurements are first converted to dose to water using the Zeiss method (Eq. 2.26) in Figure 4–1, and then the C_Q method (Eq. 2.28) in Figure 4–2, and are normalized at a depth of 1 cm. C_Q values at the PTW 34013 ionization chamber for the INTRABEAM energies were provided by Watson *et al* [33] for a range of depths from 2 mm to 35 mm. In order to use the correction factor C_Q for all the measurements, an extrapolation from a C_Q fitting curve was employed to complete data up to 50 mm. The results of the dose corrections at the extrapolated depths are indicated in *green* in Figure 4–2.

In Figure 4–1, deviations of up to 18 % from MC to the Zeiss method are observed at the closest position of 2 mm from the *Source* 1 tip. Relative differences from MC to the Zeiss method for *Source* 1 vary from -13.1 % to 3.6 % in the depth range of

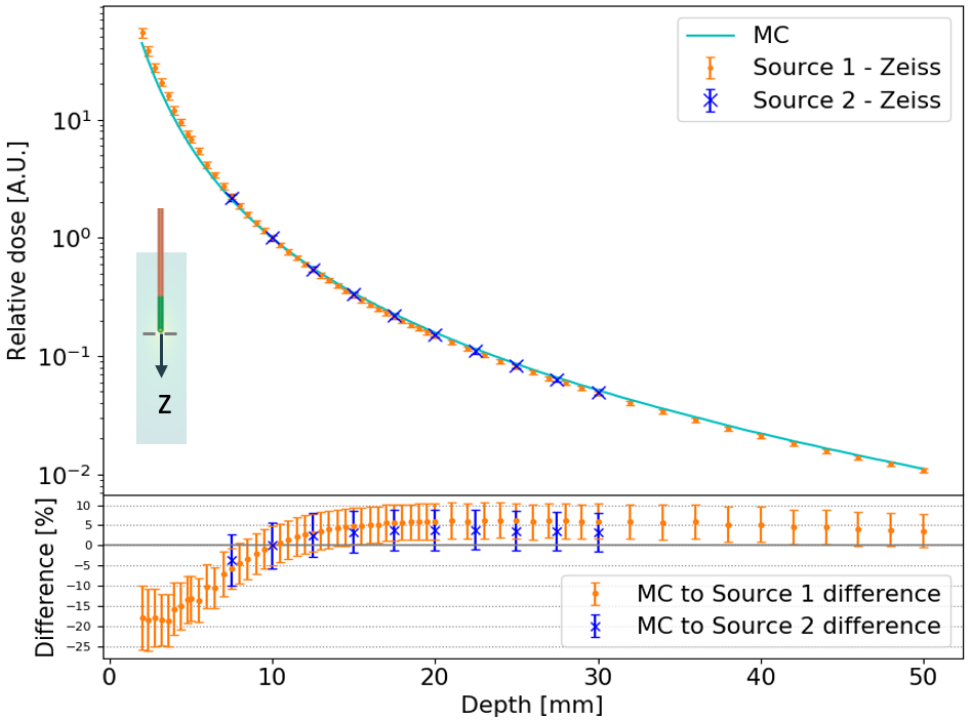

Figure 4–1 – Comparison of the MC calculated depth doses in water for the INTRABEAM against the measurements in the Zeiss Water Phantom using the PTW 34013 ionization chamber and an INTRABEAM source (*Source* 1) and the measurements with a second source (*Source* 2) by Watson *et al.* (2017) [33]. Dose to water from the measurements were obtained using the Zeiss method. All curves are normalized to 1.0 at a depth of 1 cm from the source tip. The deviation from MC simulations to measurements with both sources is shown below.

5 to 50 mm. For *Source* 2, these variations occur within −3.6 and 3.0 %, which fall within the measurement uncertainties. In a similar way, Figure 4–2 shows deviations of MC from measurements with *Source* 1 of up to 23 % when using the C_Q method, and relative differences ranging from −14.8 % to 8.7 % in the same range of depths of 5 to 50 mm. On the other hand, MC deviations from the measurements with

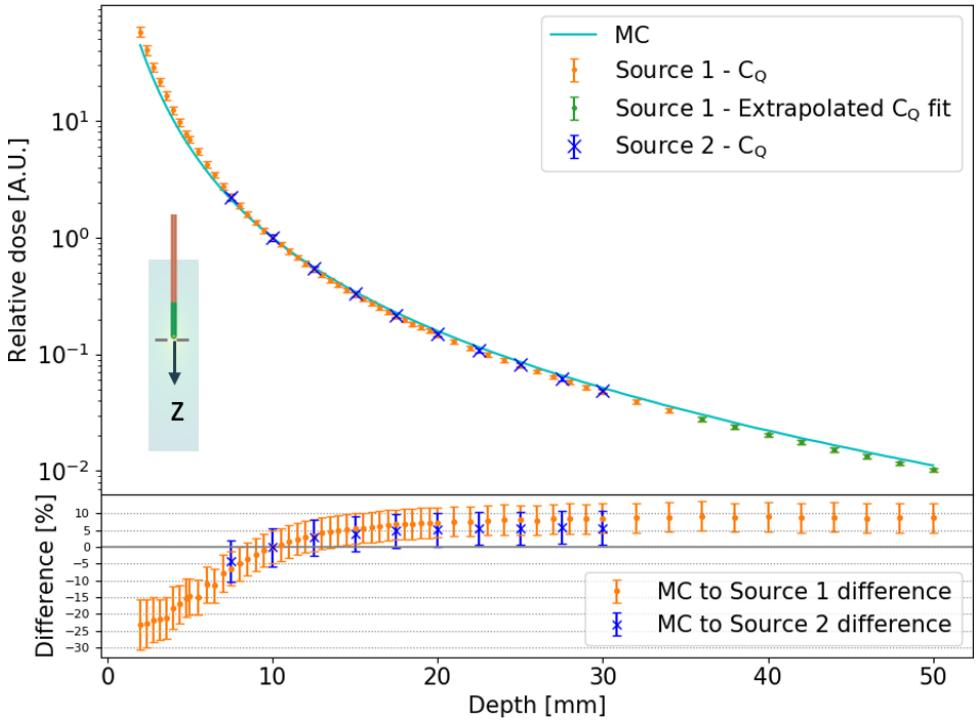

Figure 4–2 – Comparison of the MC calculated depth-doses in water for the INTRABEAM against the measurements in the Zeiss Water Phantom using the PTW 34013 ionization chamber and an INTRABEAM source (*Source* 1) and the measurements with a second source (*Source* 2) by Watson *et al.* (2017) [33]. Dose to water from the measurements were obtained using the C_Q method. Points in green indicate extrapolation from the C_Q fitting curve. All curves are normalized at a depth of 1 cm from the source tip. Deviation from MC simulations are shown below.

Source 2 vary from $-4.2\,\%$ to $6.3\,\%$ in the depth range of 7.5 to 35 mm, which fall within the corresponding measurement uncertainties.

Measurements close to the source tip are difficult to reproduce due to the rapid fall-off of the dose. In this region, uncertainties due to positioning are higher than other factors, with higher impact in the dose estimation. The discrepancies observed in Figures 4–1 and 4–2 for points closer than 5 mm to the source manifest these

difficulties which can be attributed to different dosimetric factors. Among these factors, averaging volume effects occur as the dose varies considerably over the finite RSV of the detector. In addition, the energy spectrum of the low-energy kV x-rays varies significantly with measuring depth, as the beam hardens, with demonstrated variations of HVLs of 0.1 to 2 mm Al over a distance of 2 cm [33], and this can affect the performance of the selected dosimeter. Furthermore, the C_Q method is dependent on the geometry of the ionization chamber employed, which for the PTW 34013 model, represents a significant source of uncertainty [33, 34].

For both dose estimation methods, the *Source* 2 presented better agreement with MC calculations than *Source* 1. These variations observed in the dose rate outputs for different sources have also been reported in other studies [71, 26], and can result from differences in manufacturing of the source parts involved in the x-ray beam generation and the ideal geometry modeled in the MC codes. Among the relevant components, the gold target thickness and shape and the electron source, as determined by the electron gun and the magnetic deflector, must be considered. The aforementioned differences affect the beam effective energy and slightly change the spectrum at the source or applicator output, and are reflected in the depth dose curves as variations in the beam penetration power.

Depth dose curves were also calculated and measured with the spherical applicators. Even though different sizes were studied, only the results for the 4 cm diameter applicator, which represents the most commonly used for breast and brain cancer in our clinic, are presented. In this case, depth dose curves are shown in Figure 4–3 where measurements, converted to absorbed dose with the C_Q and Zeiss

methods, are compared with MC simulations. All the curves are normalized to 1.0 at 2 mm from the applicator surface, which is the closest measurable distance due to the ionization chamber dimensions and EPOM location. Extrapolation of the C_Q data was also applied. Since measurements with the applicator start further from the source, where dose gradients are reduced, discrepancies between measurements using both methods and the MC simulations diminishes, falling close to the calculated uncertainties along the range of depths evaluated.

A possible source of error in the measurements with the applicator may be due to the use of the same C_Q values from fitted bare probe data, since C_Q might vary as a result of the change in beam quality caused by the presence of the applicator. However, previous investigations of Watson *et al* [34] have shown that the variations in the beam quality with the use of the different applicators lead to variations in C_Q values of less than 3 % *at the depth of the applicator surface.* Further research is required, however, to assess the C_Q variations due to applicator spectral hardening at depths different from applicator surface.

4.1.2 Measurements With Diamond Dosimeter

Results of the MC simulations of dose to water were also compared with measurements using the PTW TN60019 microDiamond detector and the Wellhöfer water phantom and scanning system as shown in Figure 4–4. Previous measurements with the ionization chamber, using the C_Q method to convert to dose to water, are also shown for comparisons.

Measurements with the microDiamond were first corrected with the factor C^w_{dia} of Eq. 3.2. The dose to a small volume of water and the dose to diamond required

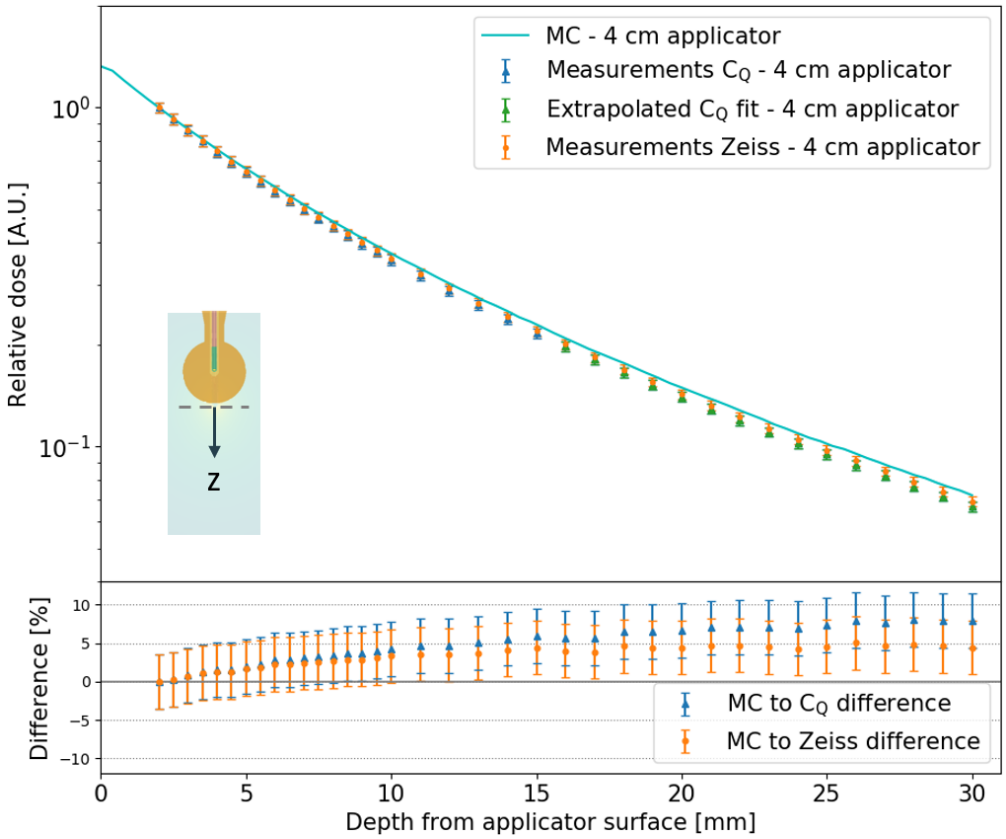

Figure 4–3 – Comparison of the MC calculated depth doses in water for the INTRABEAM with a 4 cm diameter spherical applicator against the measurements in the Zeiss Water Phantom using the PTW 34013 ionization chamber. Dose to water from the measurements were obtained using the C_Q method (*blue* + *green*) and the Zeiss method (*orange*). All curves are normalized to 1.0 at a depth of 2 mm from the applicator surface (closest measurable position). The deviation from MC simulations to measurements with both methods is shown below.

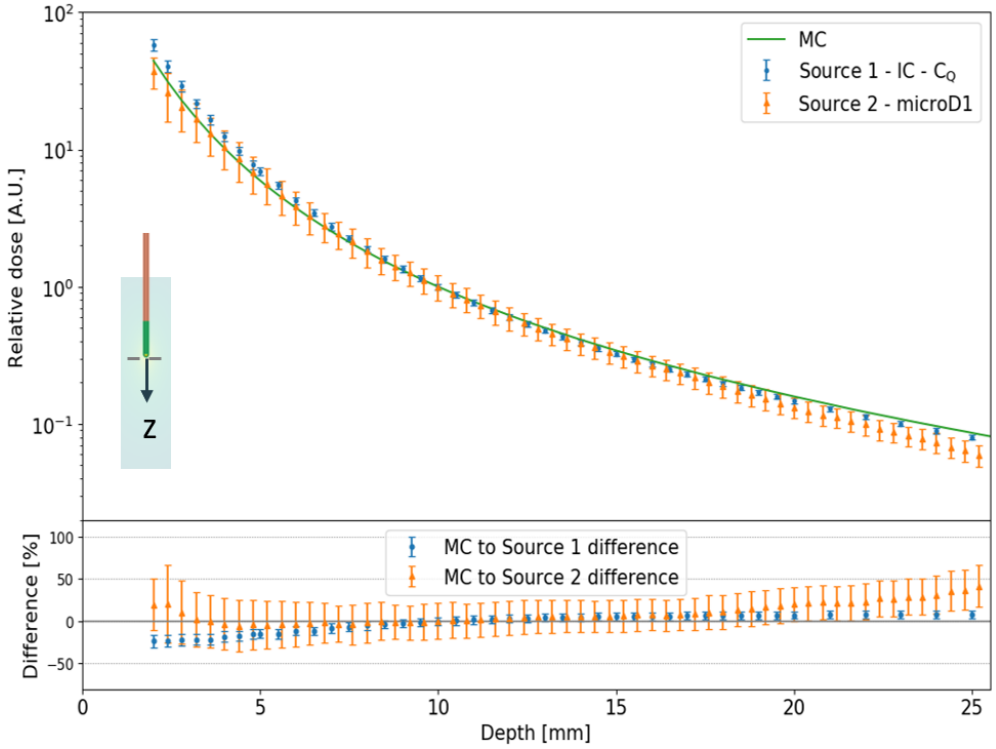

Figure 4–4 – Comparison of the MC calculated depth doses in water for the INTRABEAM against the measurements with the Wellhöfer 2D scanning system using the PTW TN60019 microDiamond detector. Dose to water from the measurements were obtained using the C^{w}_{dia} correction factor from Eq. 3.2. Previous results with the ionization chamber, using the C_Q method are also shown for comparison. All curves are normalized to 1.0 at a depth of 1 cm from the source tip. The deviation from MC simulations to measurements with both methods is shown below.

to obtain the C^w_{dia} factor were simulated with egs_chamber and the results over the range 2 to 25 mm are shown in Figure 4–5. The C^w_{dia} data was fit to a grade 6 polynomial fitting curve shown in *orange* in Figure 4–5. As expected, the C^w_{dia} factor has much higher significance for points close to the source due to the higher dose gradients and more pronounced changes in the energy spectrum, which change the mass attenuation coefficient ratios affecting the diamond readings.

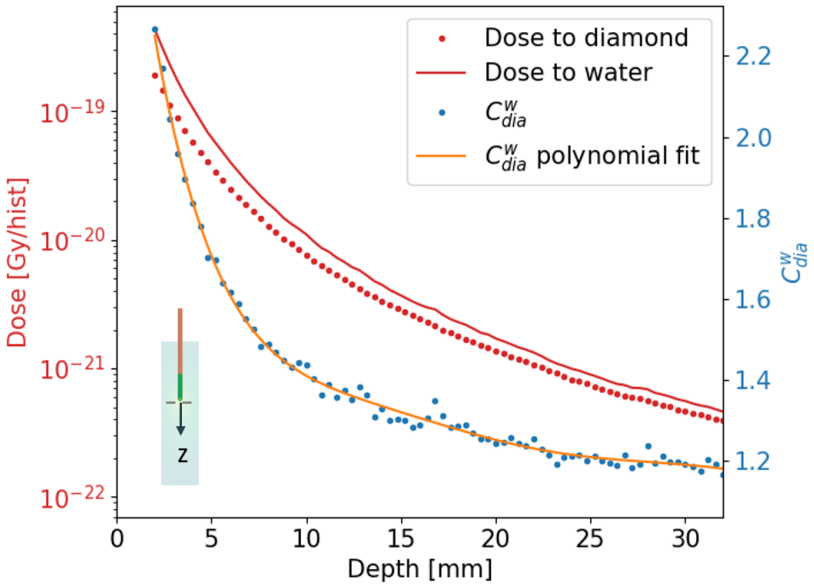

Figure 4–5 – The C^w_{dia} correction factor and a grade 6 polynomial fitting curve (*blue* points and continuous *orange* curve, with axis on the *right*) is shown, as a function of depth, together with the dose to water and dose to diamond obtained with egs_chamber (*red* curves with axis on the *left*).

After applying the C^w_{dia} correction factor to the measurements, agreement with the MC simulations is observed in the range of depths presented in Figure 4–4 within uncertainties. However, positioning uncertainties with the new system were higher since the INTRABEAM source is manually adjusted in a vertical position right above

and parallel to the detector location and displacement, and were given a 0.5 mm uncertainty in source position, as compared with the 0.1 mm uncertainty achieved with the Zeiss Water Phantom. Accounting for these uncertainties, better agreement was observed with the microDiamond at closer distances from the source tip than the results with the ionization chamber. Nevertheless, larger discrepancies were observed when moving to further positions, presumably due to decreased signal and leakage current in the detection system. To further investigate this effects, a second, more sensitive electrometer (*Keithley 6517A*) was employed, and the results are shown in Figure 4–6.

The results with the Keithley and the Wellhöfer electrometers corroborate the hypothesis of a low detection response at low dose rates present at higher depths when using the Wellhöfer electrometer, and did not significantly affect the measurements with the Keithley electrometer.

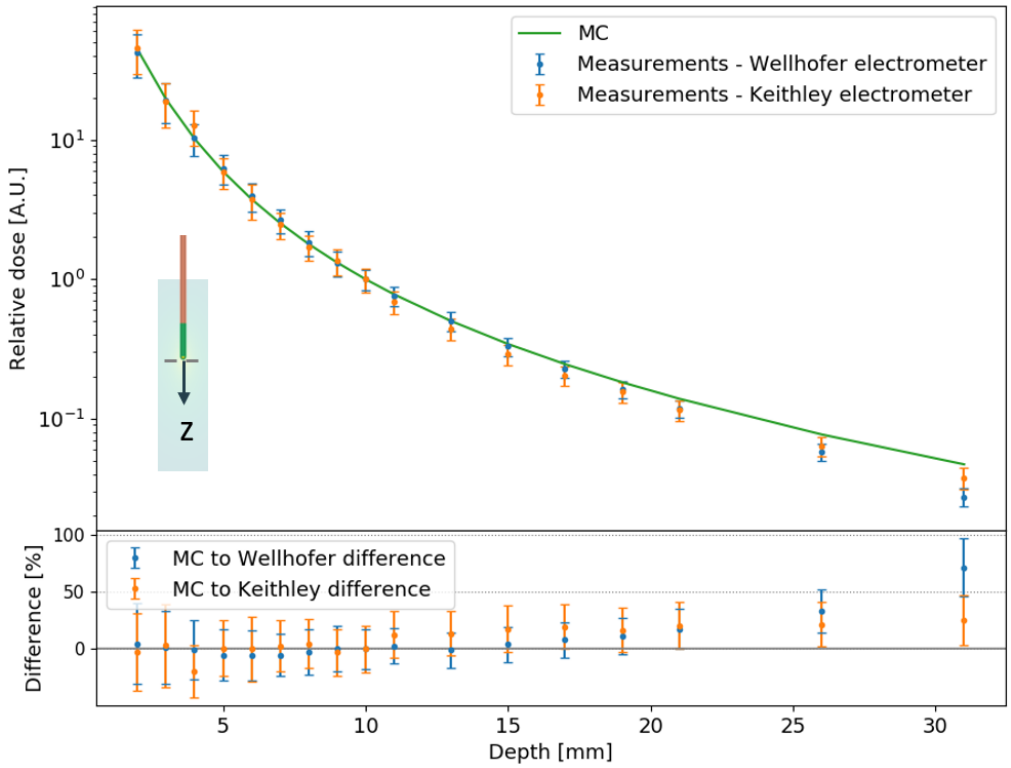

Figure 4–6 – Comparison of the MC calculated depth doses in water for the INTRABEAM against the measurements using the PTW TN60019 microDiamond detector. The results with two electrometers, a Keithley 6517A (*orange*) and a Wellhöfer CU500E (*blue*), are compared. Dose to water from the measurements were obtained using the C^{w}_{dia} correction factor from Eq. 3.2. All curves are normalized to 1.0 at a depth of 1 cm from the source tip. The deviation from MC simulations to measurements with both methods is shown below.

4.2 Radial Dose Function

The MC simulated radial dose function data for the bare probe of the INTRABEAM is presented in Table A–1 for distances to source tip ranging from 0.2 to 5.0 cm at a polar angle $\theta = 90\,^{\circ}$. The functional behaviour can be analyzed from the curve in Figure 4–7 when compared to the radial dose function reported for the Xoft source [18] operated at 50 kV and some common brachytherapy radionuclides described in the AAPM TG-43U1 report [36]. When compared to the other sources, the dose rate from the INTRABEAM source decreases with a higher steep gradient close to the source surface and then, after ∼2 cm depth, the fall-off slope becomes similar to that of the Xoft and the ^{125}I sources. The divergence from the Xoft source can be explained based on the different materials and geometries employed in the manufacturing of the source target, walls, filters and biocompatible layers, with the target material of gold for INTRABEAM and tungsten for Xoft being the main contributing factor. Different studies have shown the spectra of the INTRABEAM with predominant fluorescence peaks observed at the L-lines of gold (in the range 9.2 to 14.0 keV) and K-lines of nickel (7.5 and 8.3 keV), and a mean photon energy of ∼19 keV at the source tip [33, 23, 68, 26]. For the Xoft source, fluorescence peaks at the K-lines of yttrium (15 and 17 keV) in the tungsten anode substrate are predominant, and a mean photon energy of ∼26.7 keV for the beam output is reported [18]. At higher energies, the spectra for both sources is similar. The lower mean energy at the output of the INTRABEAM source, followed by beam hardening, explains this behaviour as compared with the Xoft source. The Type A uncertainties with

coverage factor 1 ($k = 1$) of the MC simulations varied from 0.013 % to 0.018 % at radial distances of 0.2 to 5 cm.

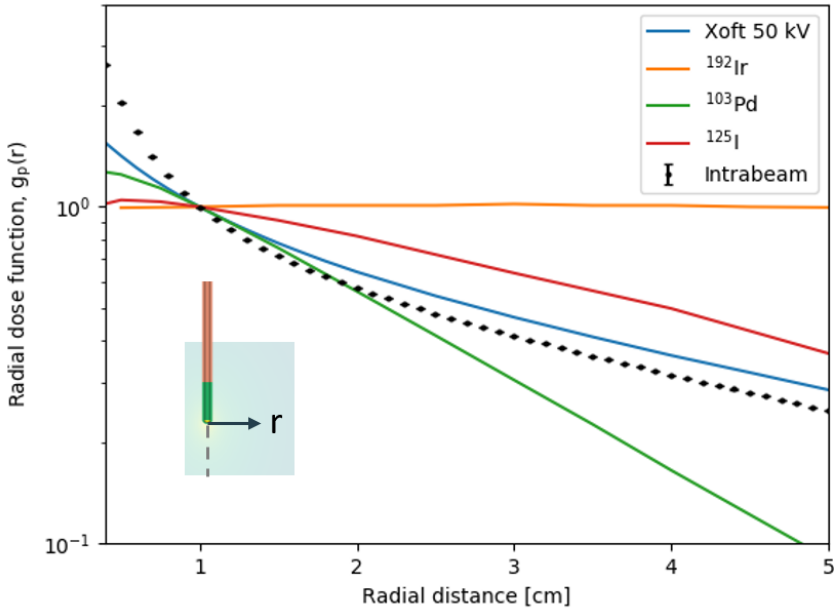

Figure 4–7 – Radial dose function for the INTRABEAM compared to results for the Xoft source operated at 50 kV [18] and common brachytherapy sources ^{192}Ir, ^{103}Pd and ^{125}I.

4.3 Anisotropy Function

The anisotropy function, shown in Figure 4–8, shows larger variations close to the source due in part to the steep gradient observed at small distances from the source tip, and attenuation in the source materials at distances larger than 1.6 cm from the tip, where the beryllium window is replaced by nickel walls. Calculated data is presented in the appendix in Table A–2 for polar angles 0° to 175° in steps of 5° and radial distances ranging from 0.2 to 5 cm. Further investigation and measurements to validate the 2D anisotropy function are recommended.

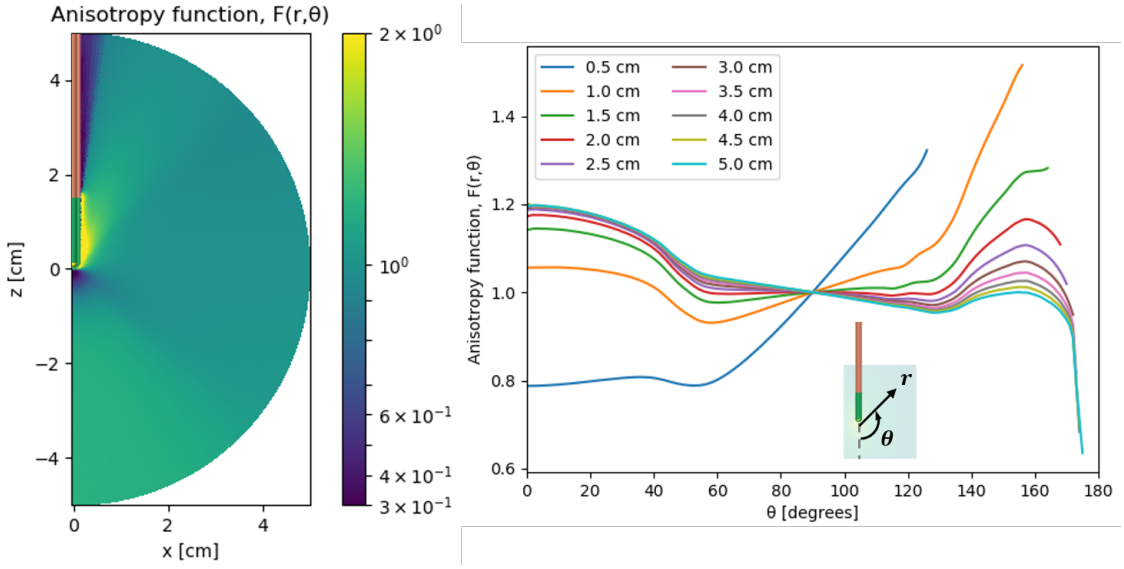

Figure 4–8 – Anisotropy function is shown for the INTRABEAM in the range $\theta = [0\,°, 180\,°]$ at different distances from the source tip.

The effect in the anisotropy function of varying the electron source from the employed ring-shape to a simpler parallel circular source was explored, and the results are compared in Figure 4–9. As observed in the MC calculations, the ring-shaped electron source might have a positive effect in isotropy around the INTRABEAM source as compared with the parallel circular source, as demonstrated by the yellow regions in the color map shown in the *right* of Figure 4–9.

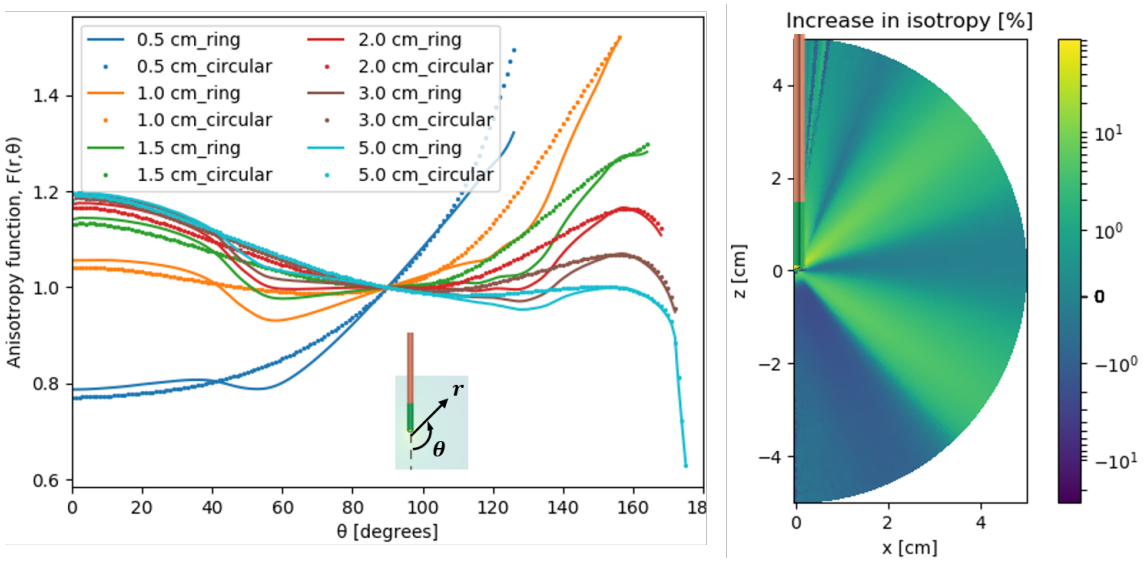

Figure 4–9 – Anisotropy function comparisons for different electron sources. In dotted curves: anisotropy function in the range $\theta = [0\,^{\circ}, 180\,^{\circ}]$ at different distances from the source tip for the parallel circular source. In continuous curves: anisotropy function results with the ring-shaped source. The color map in the *right* illustrates the percentage difference between the anisotropy function with the ring source to the results with the circular source, normalized to the distribution with the circular source.

Chapter 5
Conclusions

In this study, the radial dose function, $g_{\mathrm{p}}(r)$, and the anisotropy function, $F(r,\theta)$, recommended by the AAPM TG-43 as dosimetric parameters for brachytherapy sources, were calculated in water for the INTRABEAM miniature x-ray source using Monte Carlo simulations. The Monte Carlo model of the source was validated with depth dose measurements in water using a soft x-ray ionization chamber (PTW 34013) and a synthetic diamond detector (PTW TN60019 microDiamond).

Measurements with two different INTRABEAM sources demonstrated some variations in the source output and dosimetry from one physical source to another, due to construction differences from the ideal simulated model, corroborating the findings of other authors. The measurements with the ionization chamber showed agreement with the Monte Carlo model, within the uncertainties, in water at distances from the source of clinical relevance in the range 5 to 50 mm. However, despite no significant differences were observed with the use of spherical applicators, volume averaging effects and positioning and geometry uncertainties for the bare probe made of the verification method with the soft ionization chamber not suitable for distances closer than 5 mm from the source, with discrepancies from the Monte Carlo simulations of up to 23 % when using the C_Q method for estimation of absorbed dose to water from measurements. These issues were satisfactorily accounted for with the use of the microDiamond detector in conjunction with an accurate electrometer.

This is because of the detector's smaller RSV able to reduce the volume averaging effects and still with water equivalence in terms of energy dependence even in the range of the INTRABEAM beam quality. Nevertheless, uncertainties in positioning with the employed system are still high, and the use of a positioning frame from the source is recommended for future studies.

The results of this work validate the methodology to obtain the data necessary for the characterization of the source as required by a TPS used in clinical dose calculations and allows for dosimetric comparisons with other available sources and techniques in the search for optimal outcomes in patient-specific treatments. As a consequence of these findings, the use of the INTRABEAM as an alternative to brachytherapy sources for intraoperative radiotherapy is motivated and the possibilities for the required dosimetric verifications is extended.

Other recommendations and future work derived from the research of the present work include the calculation of TG-43 parameters for distances larger than 5 cm (15−20 cm) from the source tip. This can be performed for the bare probe for completeness, but applicator-specific parameters are desired because of their clinical relevance. The following step should be to incorporate the TG-43 parameters in a TPS, with the subsequent evaluation of the dose distributions in patient specific geometries. The use of correction factors for the differences in the mass absorbed dose coefficients from tissues to water might be required, as it is well-known that the TG-43 protocol is inaccurate in assessing dose distributions in anatomical regions with tissue inhomogeneities different from water. Studies on the biological implications of

these dose distributions in IORT procedures are necessary. In addition, the acquisition of CT or other 3D imaging modalities in the treatment setup must be evaluated in the context of dose calculations, since the surgical procedure and the insertion of the INTRABEAM applicator will displace the tumor bed and surrounding tissue. In terms of the experimental measurements, the use of a specially-designed frame to position the source in the water measurements with the microDiamond might considerably reduce the associated measuring uncertainties. Furthermore, the use of radiochromic films for 2D dose distribution and 2D anisotropy function evaluations is recommended.

Appendix A
INTRABEAM Source Radial Dose Function and Anisotropy Function Tables

Table A–1 – MC calculated radial dose function data, $g_p(r)$, using the point source approximation for the INTRABEAM source.

r[cm]	$g_p(r)$	uncertainty[%]
0.2	4.763	0.0127
0.4	2.507	0.0119
0.6	1.644	0.0107
0.8	1.232	0.0098
1.0	1.000	0.0094
1.2	0.854	0.0094
1.4	0.753	0.0095
1.6	0.678	0.0098
1.8	0.619	0.0101
2.0	0.571	0.0105
2.2	0.530	0.0108
2.4	0.495	0.0112
2.6	0.464	0.0116
2.8	0.436	0.0120
3.0	0.411	0.0125
3.2	0.388	0.0129
3.4	0.367	0.0134
3.6	0.348	0.0138
3.8	0.330	0.0143
4.0	0.313	0.0148
4.2	0.298	0.0153
4.4	0.283	0.0159
4.6	0.270	0.0164
4.8	0.257	0.0169
5.0	0.245	0.0175

Table A–2 – MC calculated 2D anisotropy function data, $F(r, \theta)$, for the bare probe of the INTRABEAM source. Points located inside the source, for which $F(r, \theta)$ is not determined, are indicated by 'NA'.

	Radial distance, r [cm]								
Polar angle, θ [°]	0.2	0.4	0.6	0.8	1	2	3	4	5
0	0.394	0.686	0.868	0.982	1.056	1.172	1.192	1.199	1.199
5	0.395	0.686	0.869	0.983	1.056	1.175	1.192	1.195	1.196
10	0.399	0.689	0.870	0.984	1.057	1.172	1.189	1.192	1.192
15	0.404	0.693	0.873	0.984	1.055	1.167	1.183	1.186	1.187
20	0.410	0.699	0.875	0.983	1.052	1.160	1.175	1.178	1.179
25	0.417	0.706	0.876	0.981	1.047	1.150	1.165	1.168	1.169
30	0.428	0.712	0.877	0.977	1.040	1.138	1.152	1.155	1.156
35	0.441	0.718	0.876	0.970	1.029	1.122	1.136	1.139	1.140
40	0.453	0.721	0.869	0.957	1.012	1.099	1.114	1.118	1.120
45	0.467	0.721	0.854	0.933	0.982	1.064	1.080	1.087	1.091
50	0.485	0.721	0.840	0.910	0.953	1.029	1.048	1.057	1.064
55	0.509	0.728	0.834	0.895	0.934	1.004	1.024	1.035	1.043
60	0.541	0.746	0.842	0.897	0.932	0.997	1.016	1.026	1.034
65	0.584	0.775	0.860	0.909	0.939	0.996	1.013	1.022	1.028
70	0.640	0.811	0.884	0.925	0.950	0.997	1.010	1.018	1.022
75	0.707	0.852	0.911	0.942	0.962	0.999	1.008	1.014	1.017
80	0.786	0.898	0.939	0.961	0.975	1.000	1.006	1.009	1.012
85	0.883	0.947	0.969	0.981	0.988	1.000	1.003	1.005	1.006
90	1.000	1.000	1.000	1.000	1.000	1.000	1.000	1.000	1.000
95	NA	NA	1.031	1.019	1.012	1.000	0.997	0.995	0.994
100	NA	NA	1.063	1.037	1.023	1.000	0.993	0.990	0.988
105	NA	NA	1.094	1.057	1.035	0.998	0.989	0.985	0.982
110	NA	NA	1.127	1.076	1.046	0.996	0.984	0.979	0.976
115	NA	NA	1.159	1.093	1.054	0.992	0.980	0.974	0.969
120	NA	NA	1.187	1.107	1.066	0.997	0.979	0.970	0.965
125	NA	NA	1.235	1.148	1.093	0.996	0.973	0.963	0.957
130	NA	NA	1.318	1.191	1.119	1.001	0.973	0.961	0.954
135	NA	NA	1.440	1.270	1.178	1.026	0.988	0.971	0.962
140	NA	NA	NA	1.389	1.268	1.070	1.018	0.994	0.979
145	NA	NA	NA	1.503	1.351	1.107	1.041	1.009	0.990
150	NA	NA	NA	NA	1.425	1.135	1.056	1.019	0.997
155	NA	NA	NA	NA	1.504	1.160	1.068	1.026	1.000
160	NA	NA	NA	NA	NA	1.161	1.064	1.020	0.994
165	NA	NA	NA	NA	NA	1.138	1.040	1.000	0.976
170	NA	NA	NA	NA	NA	NA	0.989	0.956	0.938
175	NA	NA	NA	NA	NA	NA	NA	NA	0.635

References

[1] Canadian Cancer Statistics Advisory Committee. Canadian Cancer Statistics 2018. Toronto, ON. Available at: cancer.ca/Canadian-Cancer-Statistics-2018-EN (accessed June 2019). *Canadian Cancer Society*, 2018.

[2] Freddie Bray, Jacques Ferlay, Isabelle Soerjomataram, Rebecca L. Siegel, Lindsey Torre, and Ahmedin Jemal. Global Cancer Statistics 2018: GLOBOCAN Estimates of Incidence and Mortality Worldwide for 36 Cancers in 185 Countries. *CA: A Cancer Journal for Clinicians*, 68, 09 2018.

[3] RadiologyInfo.org. Introduction to Cancer Therapy (Radiation Oncology). Available at: https://www.radiologyinfo.org/en/info.cfm?pg=intro_onco (accessed June 2019). *RadiologyInfo.org*, 2019.

[4] M.C. Joiner and A. van der Kogel. *Basic Clinical Radiobiology, Fifth Edition.* Taylor & Francis, 2016.

[5] E.B. Podgoršak and International Atomic Energy Agency. *Radiation Oncology Physics: A Handbook for Teachers and Students.* STI/PUB. International Atomic Energy Agency, 2005.

[6] C.-M. Ma, C. W. Coffey, L. A. DeWerd, C. Liu, R. Nath, S. M. Seltzer, and J. P. Seuntjens. AAPM protocol for 40-300 kV x-ray beam dosimetry in radiotherapy and radiobiology. *Medical Physics*, 28(6):868–893, 2001.

[7] Faiz M. Khan and John P. Gibbons. *Khan's The Physics of Radiation Therapy.* Wolters Kluwer Health, 2014.

[8] J. T. Bushberg and J. A. Seibert. *Essential Physics of Medical Imaging.* Wolters Kluwer Health, 3 edition, 2012.

[9] Frank W. Hensley. Present state and issues in IORT Physics. *Radiation Oncology*, 12(1), 2017.

[10] Jatinder R. Palta, Peter J. Biggs, John D. Hazle, M.Saiful Huq, Robert A. Dahl, Timothy G. Ochran, Jerry Soen, Ralph R. Dobelbower, and Edwin C. McCullough. Intraoperative electron beam radiation therapy: Technique, dosimetry, and dose specification: Report of task force 48 of the radiation therapy committee, American Association of Physicists in Medicine. *International Journal of Radiation Oncology*Biology*Physics*, 33(3):725–746, 1995.

[11] A. Sam Beddar, Peter J. Biggs, Sha Chang, Gary A. Ezzell, Bruce A. Faddegon, Frank W. Hensley, and Michael D. Mills. Intraoperative radiation therapy using mobile electron linear accelerators: Report of AAPM Radiation Therapy Committee Task Group No. 72. *Medical Physics*, 33(5):1476–1489, 2006.

[12] Jayant S Vaidya, Frederik Wenz, Max Bulsara, Jeffrey S Tobias, David J Joseph, Mohammed Keshtgar, Henrik L Flyger, Samuele Massarut, Michael Alvarado, and Christobel et al. Saunders. Risk-adapted targeted intraoperative radiotherapy versus whole-breast radiotherapy for breast cancer: 5-year results for local control and overall survival from the TARGIT-A randomised trial. *The Lancet*, 383(9917):603–613, 2014.

[13] Frank A. Giordano, Stefanie Brehmer, Yasser Abo-Madyan, Grit Welzel, Elena Sperk, Anke Keller, Frank Schneider, Sven Clausen, Carsten Herskind, Peter Schmiedek, and Frederik Wenz. INTRAGO: intraoperative radiotherapy in glioblastoma multiforme – a Phase I/II dose escalation study. *BMC Cancer*, 14(1):992, Dec 2014.

[14] Frank A Giordano, Stefanie Brehmer, Bettina Mürle, Grit Welzel, Elena Sperk, Anke Keller, Yasser Abo-Madyan, Elisabeth Scherzinger, Sven Clausen, and Frank et al. Schneider. Intraoperative Radiotherapy in Newly Diagnosed Glioblastoma (INTRAGO): An Open-Label, Dose-Escalation Phase I/II Trial. *Neurosurgery*, 84(1):41–49, 2018.

[15] G. Glatting, S. Clausen, and F. Wenz. Intraoperative radiation therapy. *Zeitschrift fur Medizinische Physik*, 24(1):1–2, 2014.

[16] Catherine C. Park, Sue S. Yom, Matthew B. Podgorsak, Eleanor Harris, Robert A. Price, Alison Bevan, Jean Pouliot, Andre A. Konski, and Paul E. Wallner. American Society for Therapeutic Radiology and Oncology (ASTRO) Emerging Technology Committee Report on Electronic Brachytherapy. *International Journal of Radiation Oncology*Biology*Physics*, 76(4):963–972, 2010.

[17] DJ Eaton. Electronic brachytherapy—current status and future directions. *The British journal of radiology*, 88(1049):20150002, 2015.

[18] Mark J. Rivard, Stephen D. Davis, Larry A. DeWerd, Thomas W. Rusch, and Steve Axelrod. Calculated and measured brachytherapy dosimetry parameters in water for the Xoft Axxent X-Ray Source: An electronic brachytherapy sourcea). *Medical Physics*, 33(11):4020–4032, 2006.

[19] Derek Liu, Emily Poon, Magdalena Bazalova, Brigitte Reniers, Michael Evans, Thomas Rusch, and Frank Verhaegen. Spectroscopic characterization of a novel electronic brachytherapy system. *Physics in Medicine and Biology*, 53(1):61–75, dec 2007.

[20] Robert M Douglas, John Beatty, Kenneth Gall, Raul F Valenzuela, Peter Biggs, Paul Okunieff, and Francisco S Pardo. Dosimetric results from a feasibility study of a novel radiosurgical source for irradiation of intracranial metastases. *International journal of radiation oncology, biology, physics*, 36(2):443–450, 1996.

[21] Leonard L Gunderson, Christopher G Willett, Felipe A Calvo, and Louis B Harrison. *Intraoperative irradiation: techniques and results*. Springer Science & Business Media, 2 edition, 2011.

[22] M. Dinsmore, K. J. Harte, A. P. Sliski, D. O. Smith, P. M. Nomikos, M. J. Dalterio, A. J. Boom, W. F. Leonard, P. E. Oettinger, and J. C. Yanch. A new miniature x-ray source for interstitial radiosurgery: Device description. *Medical Physics*, 23(1):45–52, 1996.

[23] J. C. Yanch and K. J. Harte. Monte Carlo simulation of a miniature, radiosurgery x-ray tube using the ITS 3.0 coupled electron-photon transport code. *Medical Physics*, 23(9):1551–1558, 1996.

[24] Sven Clausen, Frank Schneider, Lennart Jahnke, Jens Fleckenstein, JÃijrgen Hesser, Gerhard Glatting, and Frederik Wenz. A Monte Carlo based source model for dose calculation of endovaginal TARGIT brachytherapy with INTRABEAM and a cylindrical applicator. *Zeitschrift fÃijr Medizinische Physik*, 22(3):197–204, 2012.

[25] D S Biggs and E S Thomson. Radiation properties of a miniature X-ray device for radiosurgery. *The British Journal of Radiology*, 69(822):544–547, 1996.

[26] F Moradi, N M Ung, M U Khandaker, G A Mahdiraji, M Saad, R Abdul Malik, A Z Bustam, Z Zaili, and D A Bradley. Monte Carlo skin dose simulation in intraoperative radiotherapy of breast cancer using spherical applicators. *Physics in Medicine & Biology*, 62(16):6550–6566, 2017.

[27] Anil Sethi, Bahman Emami, William Small Jr, and Tarita O Thomas. Intraoperative radiotherapy with INTRABEAM: technical and dosimetric considerations. *Frontiers in oncology*, 8:74, 2018.

[28] Carl Zeiss Meditec AG. *INTRABEAM System from ZEISS – Technical Specifications, EN_30_010_0158IV*.

[29] DJ Eaton. Quality assurance and independent dosimetry for an intraoperative x-ray device. *Medical physics*, 39(11):6908–6920, 2012.

[30] American Association of Physicists in Medicine et al. *Statement on the Role of a Physicist in Radiation Oncology: The Report of Task Group 1 of the Professional Information and Clinical Relations Committee*. American Association of Physicists in Medicine, 1993.

[31] Carl Zeiss Meditec AG. *INTRABEAM dosimetry, Brochure EN_30_010_155II*, 2011.

[32] DJ Eaton and S Duck. Dosimetry measurements with an intra-operative x-ray device. *Physics in Medicine & Biology*, 55(12):N359, 2010.

[33] Peter G F Watson, Marija Popovic, and Jan Seuntjens. Determination of absorbed dose to water from a miniature kilovoltage x-ray source using a parallel-plate ionization chamber. *Physics in Medicine & Biology*, 63(1):015016, 2017.

[34] Peter G. F. Watson, Hamed Bekerat, Pavlos Papaconstadopoulos, Stephen Davis, and Jan Seuntjens. An investigation into the INTRABEAM miniature x-ray source dosimetry using ionization chamber and radiochromic film measurements. *Medical Physics*, 45(9):4274–4286, 2018.

[35] Ravinder Nath, Lowell L. Anderson, Gary Luxton, Keith A. Weaver, Jeffrey F. Williamson, and Ali S. Meigooni. Dosimetry of interstitial brachytherapy sources: Recommendations of the AAPM Radiation Therapy Committee Task Group No. 43. *Medical Physics*, 22(2):209–234, 1995.

[36] Mark J. Rivard, Bert M. Coursey, Larry A. DeWerd, William F. Hanson, M. Saiful Huq, Geoffrey S. Ibbott, Michael G. Mitch, Ravinder Nath, and Jeffrey F.

Williamson. Update of AAPM Task Group No. 43 Report: A revised AAPM protocol for brachytherapy dose calculations. *Medical Physics*, 31(3):633–674, 2004.

[37] David J. Thomas. ICRU report 85: fundamental quantities and units for ionizing radiation. *Radiation Protection Dosimetry*, 150(4):550–552, 05 2012.

[38] Pedro Andreo, David T Burns, Alan E Nahum, Jan Seuntjens, and Frank Herbert Attix. *Fundamentals of ionizing radiation dosimetry*. Wiley-Vch, 2017.

[39] Wolfram U Laub and Tony Wong. The volume effect of detectors in the dosimetry of small fields used in IMRT. *Medical physics*, 30(3):341–347, 2003.

[40] PTW-Freiburg. *Ionizing radiation detectors – Including codes of practice, D165.229.00/11. Available at: http://biowel.com/pdf/PTW/Detectors.pdf (accessed July 2019)*, 2018.

[41] Peter R Almond, Peter J Biggs, Bert M Coursey, WF Hanson, M Saiful Huq, Ravinder Nath, and DWO Rogers. AAPM's TG-51 protocol for clinical reference dosimetry of high-energy photon and electron beams. *Medical physics*, 26(9):1847–1870, 1999.

[42] P Andreo, DT Burns, K Hohlfeld, M Saiful Huq, T Kanai, F Laitano, V Smyth, and S Vynckier. IAEA TRS-398–Absorbed dose determination in external beam radiotherapy: an international code of practice for dosimetry based on standards of absorbed dose to water. *International Atomic Energy Agency*, 2000.

[43] Richard P Hugtenburg, Kristen Johnston, Graham J Chalmers, and Alun H Beddoe. Application of diamond detectors to the dosimetry of 45 and 100 kVp therapy beams: comparison with a parallel-plate ionization chamber and Monte Carlo. *Physics in Medicine & Biology*, 46(9):2489, 2001.

[44] S Almaviva, Marco Marinelli, E Milani, G Prestopino, A Tucciarone, C Verona, G Verona-Rinati, M Angelone, M Pillon, I Dolbnya, et al. Chemical vapor deposition diamond based multilayered radiation detector: Physical analysis of detection properties. *Journal of applied physics*, 107(1):014511, 2010.

[45] Jayde Livingstone, Andrew W Stevenson, Duncan J Butler, Daniel Häusermann, and Jean-François Adam. Characterization of a synthetic single crystal diamond detector for dosimetry in spatially fractionated synchrotron x-ray fields. *Medical physics*, 43(7):4283–4293, 2016.

[46] Marco Marinelli, G Prestopino, C Verona, and G Verona-Rinati. Experimental determination of the PTW 60019 microDiamond dosimeter active area and volume. *Medical physics*, 43(9):5205–5212, 2016.

[47] Vaiva Kaveckyte, Alexandr Malusek, Hamza Benmakhlouf, Gudrun Alm Carlsson, and Åsa Carlsson Tedgren. Suitability of microDiamond detectors for the determination of absorbed dose to water around high-dose-rate 192Ir brachytherapy sources. *Medical physics*, 45(1):429–437, 2018.

[48] Joshita Damodar, David Odgers, Dane Pope, and Robin Hill. A study on the suitability of the PTW microDiamond detector for kilovoltage x-ray beam dosimetry. *Applied Radiation and Isotopes*, 135:104–109, 2018.

[49] C Di Venanzio, Marco Marinelli, E Milani, G Prestopino, C Verona, G Verona-Rinati, MD Falco, P Bagalà, R Santoni, and M Pimpinella. Characterization of a synthetic single crystal diamond Schottky diode for radiotherapy electron beam dosimetry. *Medical physics*, 40(2):021712, 2013.

[50] ICRU. *Dosimetry of High-energy Photon Beams Based on Standards of Absorbed Dose to Water. Report 64.* International Commission on Radiation Units and Measurements, 2001.

[51] S C Klevenhagen, R J Aukett, R M Harrison, C Moretti, A E Nahum, and K E Rosser. The IPEMB code of practice for the determination of absorbed dose for x-rays below 300 kV generating potential (0.035 mm Al - 4 mm Cu HVL; 10–300 kV generating potential). *Physics in Medicine and Biology*, 41(12):2605–2625, dec 1996.

[52] RJ Aukett, JE Burns, AG Greener, RM Harrison, C Moretti, AE Nahum, and KE Rosser. Addendum to the IPEMB code of practice for the determination of absorbed dose for x-rays below 300 kV generating potential (0.035 mm Al–4 mm Cu HVL). *Physics in Medicine & Biology*, 50(12):2739–2748, 2005.

[53] DIN. *Clinical Dosimetry: Application of x rays with Peak Voltages Between 10 and 100 kV in Radiotherapy and Soft Tissue Diagnostics.* Deutsche Norm DIN 6809-4, Deutsches Institut fur Normung, Berlin (in German), 2001.

[54] DIN. *Clinical Dosimetry-Part 5: Application of x rays with Peak Voltages Between 100 and 400 kV in Radiotherapy.* Deutsche Norm DIN 6809-5, Deutsches Institut fur Normung, Berlin (in German), 2001.

[55] TWM Grimbergen, AHL Aalbers, BJ Mijnheer, J Seuntjens, H Thierens, J Van Dam, FW Wittkämper, and J Zoetelief. Dosimetry of low and medium energy x-rays-a code of practice for use in radiotherapy and radiobiology NCS Report 10. *Nederlandse Commissie voor Stralingsdosimetrie, Amsterdam*, 1997.

[56] Carl Zeiss Meditec AG. *INTRABEAM Water Phantom – Instructions for use, G-30-1767-en Version 5.0*, 2015.

[57] Larry A. DeWerd, Wesley S. Culberson, John A. Micka, and Samantha J. Simiele. A modified dose calculation formalism for electronic brachytherapy sources. *Brachytherapy*, 14(3):405–408, 2015.

[58] Joao Seco and Frank Verhaegen. *Monte Carlo techniques in radiation therapy.* CRC press, 2013.

[59] J. Wulff, K. Zink, and I. Kawrakow. Efficiency improvements for ion chamber calculations in high energy photon beams. *Medical Physics*, 35(4):1328–1336, 2008.

[60] Jeffrey Williamson. Monte Carlo evaluation of kerma at a point for photon transport problems. *Medical Physics*, 14(4):567–576, 1 1987.

[61] Sea Agostinelli, John Allison, K al Amako, John Apostolakis, H Araujo, P Arce, M Asai, D Axen, S Banerjee, G 2 Barrand, et al. GEANT4–a simulation toolkit. *Nuclear instruments and methods in physics research section A: Accelerators, Spectrometers, Detectors and Associated Equipment*, 506(3):250–303, 2003.

[62] Francesc Salvat, José M Fernández-Varea, and Josep Sempau. PENELOPE-2008: A code system for Monte Carlo simulation of electron and photon transport. In *Workshop Proceedings*, volume 4, page 7, 2006.

[63] R Arthur Forster, Lawrence J Cox, Richard F Barrett, Thomas E Booth, Judith F Briesmeister, Forrest B Brown, Jeffrey S Bull, Gregg C Geisler, John T Goorley, Russell D Mosteller, et al. MCNPâĎć version 5. *Nuclear Instruments and Methods in Physics Research Section B: Beam Interactions with Materials and Atoms*, 213:82–86, 2004.

[64] I. Kawrakow and D. W. O. Rogers. The EGSnrc code system: Monte Carlo simulation of electron and photon transport. Technical Report PIRS-701, National Research Council Canada, Ottawa, Canada, 2019.

[65] Ervin B Podgorsak. *Radiation physics for medical physicists, second edition*. Springer, 2010.

[66] Marc J P Chamberland, Randle E P Taylor, D W O Rogers, and Rowan M Thomson. egs_brachy: a versatile and fast Monte Carlo code for brachytherapy. *Physics in Medicine & Biology*, 61(23):8214–8231, 2016.

[67] I. Kawrakow, E. Mainegra-Hing, F. Tessier, and B. R. B. Walters. The EGSnrc C++ class library, NRC Report PIRS-898 (rev A). Technical report, National Research Council Canada, Ottawa, Canada, 2009.

[68] O Nwankwo, S Clausen, F Schneider, and F Wenz. A virtual source model of a kilo-voltage radiotherapy device. *Physics in Medicine & Biology*, 58(7):2363–2375, 2013.

[69] M. J. Berger, J. H. Hubbell, S. M. Seltzer, J. Chang, J. S. Coursey, R. Sukumar, D. S. Zucker, and Olsen. XCOM: Photon Cross Sections Database (version 1.5). [Online] Available: http://physics.nist.gov/xcom (accesed March 2019). *National Institute of Standards and Technology, Gaithersburg, MD*, 2010.

[70] Jessica R. Hiatt, Stephen D. Davis, and Mark J. Rivard. A revised dosimetric characterization of the model S700 electronic brachytherapy source containing an anode-centering plastic insert and other components not included in the 2006 model. *Medical Physics*, 42(6Part1):2764–2776, 2015.

[71] Kris S Armoogum, John M Parry, Salam K Souliman, David G Sutton, and Colin D Mackay. Functional intercomparison of intraoperative radiotherapy equipment–Photon Radiosurgery System. *Radiation Oncology*, 2(1):11, 2007.